VALIDATING I123 SPECT QUANTIFICATION USING MONTE CARLO SIMULATION

by

Sara Shirazi

B.S., in Medical Electronics, B.M.S. College of Engineering, 2003
M.S., in Digital Electronics, Sharif University of Technology, 2013

Submitted to the Institute of Biomedical Engineering
in partial fulfillment of the requirements
for the degree of
Master of Science
in
Biomedical Engineering

Boğaziçi University
2025

VALIDATING I123 SPECT QUANTIFICATION USING MONTE CARLO SIMULATION

APPROVED BY:

Prof. Dr. Albert Güveniş .....
(Thesis Advisor)

Prof. Dr. Duygu EGE .....

Dr. İmran GÖKER .....

DATE OF APPROVAL: 23 September 2024

ACKNOWLEDGMENTS

I would like to express my deepest gratitude to my supervisor, Professor Albert Guvenis, for his invaluable guidance, support, and encouragement throughout this research. His expertise and insights have been instrumental in the completion of this thesis.

In addition, I would like to express appreciation to our institution's staffs for their help and collaboration during the project's stages. I would especially like to thank my family and friends for their patience and constant support throughout this journey. I could not have completed this task without their support and affection.

Finally, I would like to acknowledge the use of the SIMIND software and the detailed manual provided, which were crucial for my simulations and analyses.

Thank you all for your contributions and support.

ACADEMIC ETHICS AND INTEGRITY STATEMENT

I, Sara Shirazi, declare that the ethical research techniques and standards of academic integrity are fully embodied in this thesis. The presented data, results, and analyses are all unique and faithfully represent the conclusions of my research. All cited works were given the appropriate citations, and any collaborative efforts have been duly acknowledged. The study adheres to the ethical standards established by my university, promising honesty, transparency, and responsibility all along the research journey. A disclosure of any possible conflicts of interest has been made. The highest standards of academic ethics are upheld in this work.

Name : Signature:

_____ _____

Date:

_____

ABSTRACT

VALIDATING I123 SPECT QUANTIFICATION USING MONTE CARLO SIMULATION

The accurate quantification of I-123 Single Photon Emission Computed Tomography (SPECT) is essential for the diagnosis and ongoing observation of neurological diseases. This work compares the performance of two gamma cameras (A and B) with the goal of validating the quantification accuracy of I-123 SPECT through Monte Carlo simulations with the Zubal brain phantom, using the SIMIND. The OSEM technique was utilized to rebuild the SPECT images, which allowed for measurements of the mean activity concentration and standard deviation in specific brain regions. The quantification accuracy was evaluated by calculating the recovery coefficient (RC) and computing the uptake in the regions of the cerebellum, temporal lobe, and parietal lobe. By comparing results with known activity concentrations and taking into account the impacts of scatter correction, PVE and collimator settings, the accuracy of the simulation was evaluated. The results show that quantification errors are acceptable for both cameras. Both cameras are suitable for I-123 imaging, but the choice may depend on the specific requirements of the imaging study. Further, the study explores into the effects of different imaging parameters on quantification accuracy, providing useful insights for enhancing SPECT protocols in the context of neurological imaging.

Keywords: I-123 SPECT, Monte Carlo, Zubal Phantom, SIMIND, OSEM, LEHR, Quantification Accuracy.

ÖZET

MONTE CARLO SIMÜLASYONU KULLANARAK I-123 SPECT KANTIFIKASYONUNUN DOĞRULANMASI

I-123 Tek Foton Emisyon Bilgisayarlı Tomografi (SPECT) görÃ¼ntÃ¼lerinin doğru nicel analizi, nörolojik hastalıkların teşhisi ve izlenmesi aÃ§ısından hayati önem taşımaktadır. Bu Ã§alışma, Zubal beyin fantomu ve SIMIND kullanılarak yapılan Monte Carlo simÃ¼lasyonları aracılığıyla I-123 SPECT nicel doğruluğunu doğrulamak amacıyla iki gama kamerasının (A ve B) performansını karşılaştırmaktadır. OSEM tekniği, SPECT görÃ¼ntÃ¼lerini yeniden oluşturmak iÃ§in kullanılmış ve belirli beyin bölgelerindeki ortalama aktivite konsantrasyonu ve standart sapmanın ölÃ§Ã¼lmesini sağlamıştır. Nicel doğruluk, iyileşme katsayısının (RC) hesaplanması ve beyincik, temporal lob ve parietal lob bölgelerindeki tutulumun hesaplanması ile değerlendirilmiştir. Bilinen aktivite konsantrasyonlarıyla sonuÃ§ların karşılaştırılması ve saÃ§ılma dÃ¼zeltmesi, PVE ve kolimatör ayarlarının etkilerinin dikkate alınmasıyla simÃ¼lasyonun doğruluğu değerlendirilmiştir. SonuÃ§lar, her iki kamera iÃ§in de kabul edilebilir nicel hatalar olduğunu göstermektedir. Her iki kamera da I-123 görÃ¼ntÃ¼leme iÃ§in uygundur, ancak seÃ§im, görÃ¼ntÃ¼leme Ã§alışmasının özel gereksinimlerine bağlı olabilir. Ayrıca Ã§alışma, farklı görÃ¼ntÃ¼leme parametrelerinin nicel doğruluğa etkilerini araştırarak, nörolojik görÃ¼ntÃ¼leme bağlamında SPECT protokollerinin iyileştirilmesi iÃ§in faydalı bilgiler sunmaktadır.

Anahtar Sözcükler: I-123 SPECT, Monte Carlo, Zubal Fantom, SIMIND, OSEM, LEHR, Kantifikasyon Doğruluğu.

TABLE OF CONTENTS

LIST OF FIGURES

LIST OF TABLES

LIST OF SYMBOLS

Fi	The name for the Input file
Fz	The name for the Zubal file
$f_j^{(k+1)}$	The updated estimate of the image at voxel j after iteration k+1
P_{ij}	Probability that a photon emitted from voxel j is detected by detector i
y_i	The measured projection data for detector i
N	Total number of voxels
M	Total number of detectors
RU	Run the castor reconstruction
IT	Number of iterations
SU	Number of subsets
MB	Activity in the phantom
SM	Smoothing with filter
At	Time per projection
R_{sys}	System resolution
$R_{intrinsic}$	Intrinsic resolution
$R_{collimator}$	Collimator resolution
a	Measured activity concentration
A	True activity concentration

LIST OF ABBREVIATIONS

LEHR	Low Energy High Resolution
ELEGP	Extended Low Energy General Purpose
LEGP	Low Energy General Purpose
SPECT	Single Photon Emission Computed Tomography
OSEM	Ordered Subset Expectation Maximization
EM	Expectation Maximization
SNR	Signal to noise ratio
RC	Recovery Coefficient
PVE	Partial Volume Effect
PMTs	Photo Multiplier Tubes
NaI(Tl)	Thallium doped Sodium Iodide crystal
ROI	Region Of Interest
MBq	MegaBecquerel
QE	Quantification Error
SC	Scatter Correction
CT	Computed Tomography
MRI	Magnetic resonance

1. INTRODUCTION

Nuclear medicine has been a vital resource in clinical diagnostics for a long period of time, offering non-invasive understanding of the physiological and metabolic functions of the human body. One of the most popular methods is Single Photon Emission Computed Tomography (SPECT) imaging, which provides three-dimensional space radiotracer distribution visualization and quantification. This capability is especially useful for brain imaging, where knowing about radiotracer distribution is essential for the diagnosis of neurological diseases including Parkinson's disease, Alzheimer's disease, and other neurodegenerative illnesses [5],[6],[7]. The radiotracer iodine-123 (I-123) is frequently utilized in SPECT imaging because of its advantageous physical properties, which include an ideal gamma emission energy of 159 keV and a reasonable half-life [8]. The low-energy high-resolution (LEHR) collimator is frequently used in conjunction with it to produce high-resolution images that are necessary for detailed brain research. The literature provides ample evidence of the effectiveness of combining I-123 and LEHR collimators to improve contrast and resolution in brain SPECT imaging [7].

Even though SPECT is widely used for brain imaging, issues with quantification accuracy, image quality, and the trade-off between sensitivity and resolution still exist. These difficulties become more evident when comparing various imaging systems, including those created by A and B. Every system has distinct design features that affect imaging results. A result, variations in quantification accuracy, scatter correction methods, and image acquisition times, requiring a thorough analysis of these factors to optimize imaging protocols [6],[7].

This study uses the I-123 radiotracer to compare the capabilities of cameras A and B in SPECT systems for brain imaging. We assess the effect of scatter correction, collimator selection, and other system-specific parameters on quantification accuracy and image quality by comprehensive Monte Carlo simulations with the SI-

MIND software [6],[7]. A novel aspect of this work is the detailed study of voxel-based quantification errors in different brain lobes using advanced neuroimaging tools for enhancing the quantification and quality of images, including advanced reconstruction algorithms like OSEM and methods for error correction that decrease photon scatter and partial volume effects. By improving SPECT imaging's accuracy, such innovations aim to improve patient outcomes and diagnosis with greater accuracy.

The study also discusses the limitations of the existing SPECT imaging techniques and suggests novel ways to improve image reconstruction and analysis. To lower quantification errors and improve the diagnostic usefulness of SPECT imaging, we aim to optimize acquisition parameters and employ cutting-edge scatter correction algorithms. By offering practical insights into the optimization of SPECT imaging techniques, our findings hope to add to the body of information already in existence and ultimately improve the accuracy and reliability of brain imaging researches.

To sum up, this study presents novel approaches for enhancing image quantification and quality in addition to comparing the performance of cameras A and B SPECT systems. These novel techniques help eliminate artifacts and improve the overall quality of SPECT images. These techniques include optimizing parameters for OSEM iterations and subsets, applying scatter correction, and fine-tuning acquisition settings. Improving the quality of images is crucial for improving visualization of brain regions and guaranteeing accurate measurements in medical applications.

By resolving classic SPECT imaging challenges including balancing sensitivity and resolution and limiting noise, these unique methods especially those pertaining to parameter optimization improve quantification accuracy and image quality in I-123 brain imaging studies.

This study aims to progress nuclear medicine by filling gaps in existing procedures and putting forward creative alternatives that provide enhanced diagnostic skills for the evaluation and treatment of neurological disorders [6],[7].

1.1 Background and context

Nuclear medicine is an important area of medical imaging that measures and visualizes physiological processes at the molecular level using radiopharmaceuticals. Unlike other imaging modalities, which frequently only focus on anatomical structures, nuclear medicine has this capability [6]. Single Photon Emission Computed Tomography (SPECT) is a commonly used nuclear medicine technology that offers three-dimensional functional imaging, which is especially useful for detecting and treating neurological disorders. Iodine-123 (I-123), a radiotracer for brain imaging, is used in this study to assess the effectiveness of SPECT imaging systems, particularly those made by A and B [9],[10].

1.1.1 Nuclear medicine

Radioactive isotopes are used in nuclear medicine, by providing functional information about organs and tissues, to detect and treat disorders. By facilitating early detection and reliable monitoring of treatment responses, the field has greatly increased our understanding and management of diseases. The mainstay of nuclear medicine, radiopharmaceuticals, are composed of a radioactive isotope bonded to a carrier molecule that targets particular biological processes. Following administration, these compounds localize in the intended tissues and emit gamma rays, which are detectable and imageable with the use of appropriate equipment [6].

Because of its ideal physical characteristics, such as its 159 keV gamma emission energy and half-life of around 13.2 hours, iodine-123 (I-123) is a frequently utilized isotope in nuclear medicine [6]. These properties make I-123 a good choice for brain imaging, where it can be utilized to study cerebral blood flow and neurotransmitter activity, especially when neurological conditions like Parkinson's and Alzheimer's disease are present. I-123 is a useful tool for evaluating the dopaminergic pathways impacted by Parkinson's disease because of its ability to bind selectively to dopamine transporters [6],[11],[12].

Improvements in data processing algorithms, imaging technology, and radiopharmaceutical design contributed to advances in nuclear medicine and improved patient outcomes and diagnostic accuracy. By offering complementing anatomical and functional information in a single examination, hybrid imaging technologies like SPECT/CT have significantly increased the potential of nuclear medicine [2],[13].

1.1.2 SPECT imaging

A robust nuclear medicine imaging technique called Single Photon Emission Computed Tomography (SPECT) uses gamma rays emitted by radiopharmaceuticals inside the body to create three-dimensional images. By capturing these emissions from the rotating gamma camera at various angles around the patient, cross-sectional pictures showing the radiotracer's distribution can be reconstructed. This ability is especially useful in assessing dynamic physiological processes, like metabolic activity and blood flow, which are critical for the diagnosis and ongoing monitoring of many diseases [6].

When it comes to brain imaging, SPECT imaging is essential because it provides insight into metabolic activity, receptor binding, and cerebral perfusion. This modality is particularly useful for assessing diseases such as epilepsy, stroke, and neurodegenerative disorders, where diagnosis and therapy planning depend heavily on functional information. The assessment of certain neurotransmitter systems and cerebral blood flow patterns is made possible by the use of radiotracers, such as I-123, which improve SPECT's ability to get detailed images of brain activity [14].

Accurately quantifying tracer uptake and obtaining high image quality are two significant challenges in SPECT imaging. Reconstruction algorithms, detector technology, and collimator selection are some of the factors that affect this [9],[15],[16]. In brain SPECT studies, Low Energy High Resolution (LEHR) collimators are often used to maximize spatial resolution and sensitivity, which is essential for identifying small lesions and subtle changes in tracer distribution [6],[7].

The goal of the research project is to evaluate the resolution and quantification capabilities of cameras A and B SPECT systems in brain imaging using I-123. Through the analysis of these parameters, the research aims to determine the best imaging protocols and suggest improvements to current techniques, which will ultimately lead to better clinical outcomes and diagnostic accuracy in neurological imaging.

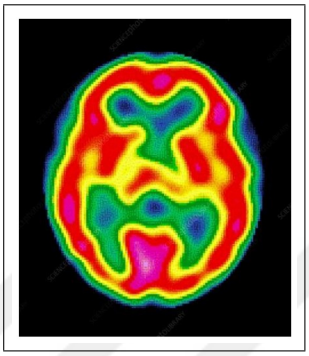

Figure 1.1 Healthy brain, SPECT scan [1]

Healthy Brain

- Uniform Uptake: The distribution of radiotracer uptake in the healthy brain is more uniform, suggesting that all areas of the brain are metabolically active normally.
- The temporal and parietal lobes: They are known for their high metabolic activity, which is reflected in their characteristic high radiotracer uptake, which is indicative of normal brain health and cognitive performance.

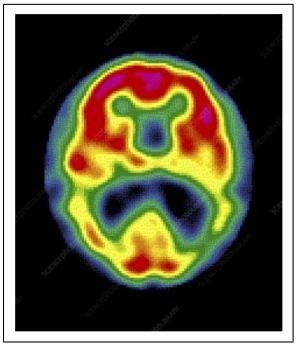

Figure 1.2 Alzheimer, SPECT scan [1]

Alzheimer's Brain

- Reduced Uptake in Temporal and Parietal Lobes: The first observable change in the early stages of Alzheimer's disease is decreased absorption in the temporal lobe, especially in the hippocampus, which is important for memory formation and retrieval. Reduced absorption spreads to the parietal lobe, which is important in navigation and spatial orientation, as the disease worsens [17].
- Advanced Stages: Later stages see a more prominent and extensive reduction in uptake, affecting not only the temporal and parietal lobes but also other areas including the frontal lobe, which increases cognitive decline and affects executive function [18]. Alzheimer's disease is one example of a neurological disorder for which this research can be used to help both identify and track its progression.

1.1.2.1 SPECT imaging fundamentals.

- Administration of Radiotracer: A patient receives an injection of a radiotracer, like I-123. Because of its capacity to attach to particular biological targets in the brain–such as dopamine transporters, which are relevant in neurological disorders–this tracer was chosen [19].
- Emission of Gamma Rays: Gamma rays emit by the radiotracer when it decays. I-123's energy and half-life make it especially well-suited for brain imaging since they make an acceptable balance between patient safety and image quality [19].
- Detection: A rotating gamma camera that collects data from various angles detects the gamma rays that emit. The distribution of the radiotracer in the brain is shown by the cross-sectional images that are created using this data [19].
- Image Reconstruction: Advanced methods are used to reconstruct the collected data into finely detailed images, such as OSEM (Ordered Subsets Expectation Maximization). These techniques reduce noise and increase resolution, which improves image quality [5],[6],[7].

- Quantification SPECT imaging provides quantitative data on radiotracer uptake in addition to qualitative images. This measurement, which compares radiotracer distribution across various brain regions, is crucial for evaluating brain function and detecting neurological disorders [20].

- Diagnosis and Monitoring: SPECT imaging helps doctors diagnose diseases like Parkinson's and Alzheimer's by allowing them to see functional changes in the brain. It also aids in tracking the progress of the condition and how well therapy is working [21].

1.1.2.2 Role of gamma cameras in medical imaging.

The core of SPECT imaging consists of gamma cameras, which are essential for both detecting and converting the gamma rays emitted by radiotracers into images that show physiological processes taking place within the body.

Components of a Gamma Camera:

- Collimator: An essential part of the system is the collimator, which filters incoming gamma rays so that only those going in certain directions can reach the detector. In my study, LEHR collimators are used to improve spatial resolution, which is essential for identifying small brain structures.

- Scintillation Crystal: The scintillation crystal, which is composed of NaI(Tl), transforms gamma rays into visible light. Subsequent detection and image generation depend on this conversion.

- Photomultiplier Tubes (PMTs): The signal from the scintillation crystal is detected by PMTs, which then amplifies the light. This signal is further processed to produce the final image.

- Electronics and Processing unit The PMT signals are processed by the gamma camera's electronics, which then reconstruct them into images that can be used for diagnostic reasons [2],[19].

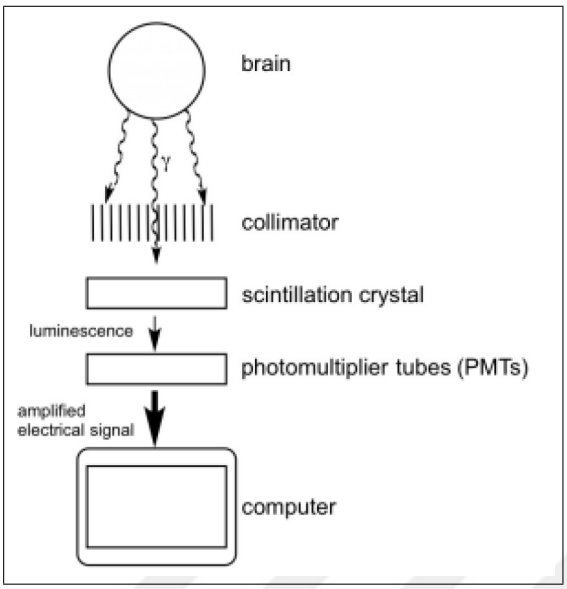

Figure 1.3 This image highlights key components of a SPECT gamma camera like a collimator, scintillation crystal, photomultiplier tubes (PMTs), and electronics that work together to detect and process the gamma photons emitted from the patient.

1.2 Problem statement

Accurate quantification of radiotracer uptake in brain regions using SPECT imaging is a crucial step in diagnosing and monitoring neurological disorders. The purpose of this study is to assess and compare the quantification accuracy of two of the top gamma camera systems, A and B, using I-123 isotope and LEHR as a collimator in the camera. Comparison is been checked in different regions of brain including the cerebellum, temporal lobe, and parietal lobe. The study seeks to provide insights into the optimal use of these systems for neurological assessments and improve diagnostic accuracy by evaluating quantification error [6],[22].

The goal of this research is to improve our knowledge and use of SPECT imaging in clinical settings by addressing these issues. To diagnose and monitor neurological disorders, accurate measurement of radiotracer uptake in brain areas is essential. But challenges including system-specific resolution and sensitivity variations, image noise, scatter, photon attenuation and partial volume effects (PVE) can make accurate measurements tricky [3],[6].

1.2.1 Absolute quantification in SPECT

In SPECT, absolute quantification involves converting image information into quantitative concentration measurements of radiotracer, expressed in MBq/ml units. This procedure is necessary to precisely evaluate brain activity and identify anomalies linked to neurological disorders.

In SPECT, absolute quantification refers to determining the amount of radiotracer uptake can be detected in a certain region of interest (ROI). Particularly in brain imaging, where subtle changes may indicate the progress of a disease or measure the efficacy of a treatment, this quantification is crucial for evaluating the functional state of tissues and organs [3],[23].

1.2.1.1 Why quantification is needed for I-123 imaging?.

In I-123 imaging, quantification is crucial because it makes it possible to monitor radiotracer uptake precisely and provides useful quantitative data in addition to the qualitative diagnostic images that are usually employed in traditional methods. Benefits of quantification in I-123 imaging:

- **Improved Accuracy:** Makes it possible to analyze radiotracer uptake detailed and detect subtle variations that can be used to diagnose neurological conditions.
- **Track Disease Progression:** uses accurate measures to assist in tracking neurological disorders over time.
- **Better Treatment Planning:** provides information for evaluating the efficacy of treatments and modifying treatment plans.
- **Objective Data:** Improves clinical decision reliability by lowering subjective variability.

This work presents new methods for improving quantification accuracy and im-

age quality in brain SPECT imaging by carefully optimizing simulation parameters and using optimal reconstruction algorithms such as OSEM.

1.3 Objectives

The following are the project's main objectives:

1.3.1 Validation

- Quantification Error Evaluation: By comparing determined uptake levels with recognized standards (mean & standard deviation), determine the quantification error for each region [16].
- Use of Phantom Data: Employ the Zubal brain phantom to validate the accuracy of the uptake measurements by comparing them to known standards [6],[7].

1.3.2 Optimization

In order to improve the accuracy and efficacy of SPECT imaging, optimization focuses on optimizing the imaging and analysis procedures:

- Adjust system parameters such as the crystal settings, system resolution, and collimator selection to minimize errors.
- Algorithm tuning: Reduce artifacts and enhance image quality by fine-tuning reconstruction techniques, such as OSEM [6],[7],[24],[25].

By accomplishing these objectives, the research hopes to improve the use of SPECT imaging in neurological diagnosis and offer suggestions for improving system configurations for more accurate quantification.

1.4 Hypothesis

Theoretically, one of these two gamma cameras which utilize the LEHR collimator and I-123 radiotracer offers better resolution and image quality than the other for brain imaging, which enables more accurate quantification of radiotracer uptake in the cerebellum, temporal lobe, and parietal lobe.

The hypothesis is based on the important role that high-resolution plays in brain imaging, particularly when using the LEHR collimator and I-123 radiotracer, which are ideal for these kinds of analyses. Resolution becomes crucial when measuring the efficacy of gamma cameras in clinical settings because of the complexity of the anatomy and the requirement for precise visualization of small structures within the brain [26].

1.4.1 Comparison of the performance of A and B gamma cameras

The project's premise is to determine whether or not A and B gamma cameras can improve resolution and imaging quality when used with I-123 and a LEHR collimator in brain studies. The objective is to figure out which system has better resolution, which is essential for precise neurological disease diagnosis and disease monitoring [27].

1.5 Scope and limitations

Study Scope

This study's main goal is to compare the performance of A and B gamma cameras for brain imaging using LEHR and I-123 collimators. The project's scope includes the following important areas:

- Gamma Camera Performance: Using I-123 and LEHR collimators, assess the gamma camera performance of A and B in terms of resolution, sensitivity, and

overall image quality [28],[29].

- Quantify Radiotracer Uptake: Analyse the precision and accuracy of radiotracer uptake measures in key brain areas, like the parietal lobe, temporal lobe, and cerebellum [30],[31].
- To improve image quality and facilitate quantitative evaluation of radiotracer uptake, apply reconstruction methods such as OSEM [5],[32].
- Resolution and Sensitivity: Evaluate and contrast each camera system's resolution and sensitivity to determine which offers greater diagnostic capabilities [33].
- Quantification Accuracy: Analyze signal-to-noise ratio (SNR) and quantification error for radiotracer uptake in specific brain areas [5].

Study Limitations

Despite the project's scope, a number of limitations need to be noted:

- Resolution vs. Sensitivity Trade-off: The trade-off between resolution and sensitivity in these systems (A vs. B) can limit the ability to achieve both high-resolution and high-sensitivity images simultaneously.
- Differences in Camera Technologies: Variations in detector technology, signal processing algorithms, and calibration procedures between A and B systems can introduce biases that need to be carefully accounted for.
- Compared to other brain regions, measuring uptake in the parietal lobe can be more difficult. Because of its variable thickness and the existence of sulci and gyri, the parietal lobe is especially exposed to the partial volume effect (PVE), which poses a serious problem for brain imaging. PVE can lead to inaccurate uptake quantification by underestimating activity in thin structures and overestimating it in thicker areas [13],[34].

These limitations suggest areas for further refinement and validation in this study. Addressing these issues might involve incorporating more diverse data, conducting sensitivity analyses, refining simulation parameters, or exploring new methodologies for quantification and optimization.

2. LITERATURE REVIEW

A nuclear imaging technology called single-photon emission computed tomography (SPECT) produces three-dimensional images of the body's functioning systems. The basic ideas behind SPECT are detecting gamma rays emitted by a radiotracer injected into the patient and reconstructing the data into cross-sectional images. The ability of SPECT imaging to detect physiological processes at the molecular level is valuable in clinical practice as it helps with the diagnosis and treatment planning of a variety of diseases, including neurological disorders [5],[6].

The literature now in publication emphasizes the complex structure of SPECT imaging in neurological applications, emphasizing both the methodological difficulties and the technology advances related to this area. This research compares the performance of the cameras A and B SPECT systems in order to clarify the relative advantages and disadvantages of each system, laying the groundwork for better imaging protocols and neurological condition diagnosis outcomes. A key component of improving brain imaging's resolution and accuracy, improving patient care, and deepening our knowledge of neurological diseases is the practical application of LEHR and I-123 collimators [5].

In a study by "Anneray Richards, a SIMIND Monte Carlo (MC) model of a gamma camera set with a Low-Energy High-Resolution (LEHR) collimator for I-123 imaging was validated. To carry out this validation, real measured data and simulated data were compared". Later the study demonstrates that LEHR is preferable for high-resolution imaging and ME for situations requiring higher sensitivity [7].

In addition to using certain ideas from previous research in a literature review, this study primarily compared its values for simulation and outcomes, according to the manufacturer values that are accessible for each camera [5],[28],[35].

2.1 System A

The A gamma camera is specialized in high-resolution imaging, and is widely recognized for its accurate collimator settings and advanced detector technology. The system A performs exceptionally well in situations where precise spatial resolution is essential, such as the imaging of small brain areas impacted by neurological diseases. Because of its design, which places an emphasis on image quality and accuracy, the system is favored by doctors who are concerned with precise diagnosis [28],[33],[36].

2.2 System B

High resolution and sensitivity are prioritized in the camera system B, which is advantageous in situations where greater count statistics and quick acquisition times are needed. The advanced electronics and materials used in this system's detector improve its capacity to collect an extensive range of photon energy with the least amount of noise. The camera B' strength is its robustness and versatility, which allow it to be used for a variety of therapeutic applications, such as dynamic investigations of brain activity [29],[32],[35],[37].

2.3 SPECT imaging resolution and sensitivity

Two essential SPECT imaging characteristics that affect image quality and diagnostic precision are resolution and sensitivity. In order to precisely localize radiotracer uptake and identify small abnormalities in brain tissue, high resolution is necessary. But sensitivity is frequently sacrificed for higher resolution, which might make it harder for the system to detect and pick up on weak radiotracer activity [2].

The Anneray Richards research considered the trade-offs between resolution and sensitivity using LEHR [7].

2.3.1 Methods for improving resolution

The literature outlines a number of methods for improving resolution, including using advanced reconstruction techniques like OSEM (Ordered Subsets Expectation Maximization) and optimizing collimator configuration. By enhancing spatial resolution without considerably sacrificing sensitivity, these techniques seek to preserve the equilibrium required for efficient imaging [6],[7],[30].

2.3.2 Techniques for sensitivity optimization

Particularly in studies requiring low radiotracer dosages or quick physiological processes, sensitivity is essential for obtaining adequate photon counts [13],[16],[8]. Using high-efficiency detectors and optimizing acquisition procedures and also using a different collimator like ME, are ways to increase sensitivity and guarantee that enough data is recorded without unnecessarily extending scan times [6],[7],[13].

2.4 I-123 and LEHR collimators used in brain imaging

Because of its ideal physical characteristics for monitoring brain activity, especially when it comes to dopamine transporters and receptors, I-123 is frequently utilized in SPECT brain imaging. With low-energy isotopes like I-123, LEHR collimators are made to function especially well, producing high-resolution images that are essential for identifying diseases like Parkinson's and Alzheimer's [14],[38].

2.4.1 Neurological studies using I-123

Studies show that I-123 is especially useful for demonstrating dopaminergic pathways, providing information on neurological disorders with modified dopamine transmission [26]. Therapeutic decision-making is aided by the early diagnosis and

tracking of disease progression made possible by the use of I-123 and advanced imaging techniques [12].

2.4.2 LEHR collimators: advantages and limitations

Because they can improve image quality and make brain structures more clearly visible, LEHR collimators are preferred. Nevertheless, the trade-offs between sensitivity and resolution, as well as possible noise increases, must be carefully considered when using them. Researches indicate that LEHR collimators can significantly enhance image quality without sacrificing diagnostic accuracy when paired with optimized imaging protocols, provide significant improvements in image quality without compromising diagnostic accuracy [7].

2.5 Quantification challenges and solutions

A crucial component of SPECT imaging is quantifying radiotracer uptake, which yields quantitative information that can be associated with clinical results. Partial volume effects, photon attenuation, and scatter are among the characteristics that make precise quantification challenging to achieve. The literature describes a number of approaches to deal with these problems, such as the application of correction algorithms and the addition of anatomical data to improve quantification [23],[39],[40].

2.5.1 Photon Attenuation And Scatter Correction

To acquire accurate quantitative data, photon attenuation and scatter must be corrected for. The accuracy of the quantification process is improved and reliable clinical decision-making is supported by the widespread usage of techniques like attenuation correction maps and scatter correction algorithms [3],[13].

2.5.2 Partial volume effects and correction

PVE happens when an imaging system's spatial resolution is too low to distinguish between surrounding tissues and tiny structures, which results in inaccurate activity evaluations This is especially important to consider when assessing uptake in small brain structures, as these structures often significantly underestimate the concentration of their activities [6],[41]. We can also consider Post-Processing, that is taking into account PVE post-reconstruction corrections, which could involve modifications based on anatomical information from CT or MRI scans.

3. METHODOLOGY

This section describes the approach taken in this study to validate the use of Monte Carlo simulations for I-123 SPECT quantification. The Anthropomorphic Digital Brain Phantom (Zubal), the radiotracer I-123, and the SIMIND Monte Carlo Simulation are among the resources that are chosen and prepared as part of the technique [8],[22].

3.1 Materials

3.1.1 Anthropomorphic digital brain phantom (Zubal)

In nuclear medicine, the Zubal phantom is a well-known anthropomorphic digital brain phantom that is used to validate imaging techniques. It offers a precise representation of the anatomy of the human brain, containing finely detailed features like the cerebellum, temporal lobe, parietal lobe, and other important areas. In order to simulate clinical settings in a safe setting and test various imaging protocols and reconstruction algorithms without subjecting patients to radiation, the Zubal phantom is required.

The characteristics of the Zubal phantom are:

Voxel-based structure: A 3D voxel grid is used to build the Zubal phantom. Each voxel corresponds to a distinct tissue type and has associated attenuation and scattering properties.

Realistic anatomy: A detailed representation of the human head and brain is included in the phantom, which makes it possible to simulate detailed anatomy features and how they affect SPECT imaging.

Customizability: Experiment design can be made more flexible by modifying the phantom to simulate different health situations, such as tumors or ischemia regions [32],[42].

Figure 3.1 Zubal Brain Phantom [2]

3.1.2 I-123

In SPECT imaging, iodine-123 (I-123) is a frequently used radiotracer, especially for brain research. Because of its appropriate half-life, low radiation exposure to the patient, and gamma emission energy, it is perfect for neurological imaging. I-123 is useful for the diagnosis of neurological disorders like Parkinson's disease since it may be used to identify a variety of compounds, such as ioflupane, which targets dopamine transporters in the brain [12],[14].

3.1.2.1 Decay.

Tellurium-123 (Te-123) is produced when I-123 decays by electron capture. Te-123 emits gamma rays with an energy of 159 keV, which is perfect for SPECT imaging. I-123 has a half-life of roughly 13.2 hours, which gives researchers enough time to do imaging experiments with the least amount of radiation exposure to the patient. In order to provide ideal image quality, the decay process is crucial to the timing and scheduling of imaging sessions.

Physical decay and biological excretion are the two main ways that radiotracers

leave the body.

1. **Physical Decay**

   Radioactive Decay: Radiotracers are chemicals that are radioactive and gradually decay by emitting radiation, such as beta particles or gamma rays. Their half-life, or the amount of time it takes for half of the radioactive atoms in the substance to decay, describes how quickly they decay. The half-lives of various radiotracers vary, and over time, the body's radioactivity decreases by this decay process. Iodine-123 (I-123), for instance, decays by gamma radiation. Imaging tools like SPECT cameras pick up the radiation that is released by the decaying radioactive atoms, which is a result of the radiotracer [43].

2. **Biological Excretion**

   Metabolism and Excretion: The body metabolizes and excretes the leftover radiotracer once it has completed its imaging function. The chemical characteristics of the radiotracer affect the excretion pathways. Most excretion of iodine-123 (I-123) occurs via the renal (urinary) pathway. After I-123 delivery, the radiotracer is absorbed by the kidneys and then removed from the body, mostly in the form of urine. Renal excretion is the main route of excretion, while small amounts may also be eliminated through the stools [43].

3.1.2.2 Source activity.

The quantity of radioactivity in the radiotracer at the time of injection or imaging is referred to as source activity. It affects the quantification accuracy, image quality, and signal strength, making it a crucial parameter in SPECT imaging. The source activity for I-123 in this study was carefully determined in accordance with the intended imaging settings and patient safety recommendations. The activity (index 25), which is the number of disintegrations per second, is commonly expressed in Becquerels (Bq). For brain imaging studies, the injected dosage of I-123 typically ranges from 111 to 185 MBq (3 to 5 mCi). The patient's weight, the imaging protocol, and the SPECT system's sensitivity are taken into consideration when adjusting the activity [43].

3.1.3 SIMIND Monte Carlo simulation

In this work, the entire SPECT imaging process including photon interactions, detector responses, and image reconstruction is simulated using the Monte Carlo simulation tool SIMIND. In nuclear medicine, Monte Carlo simulations are especially useful for simulating complicated physical processes that are challenging to quantify directly, like photon scattering and attenuation [8].

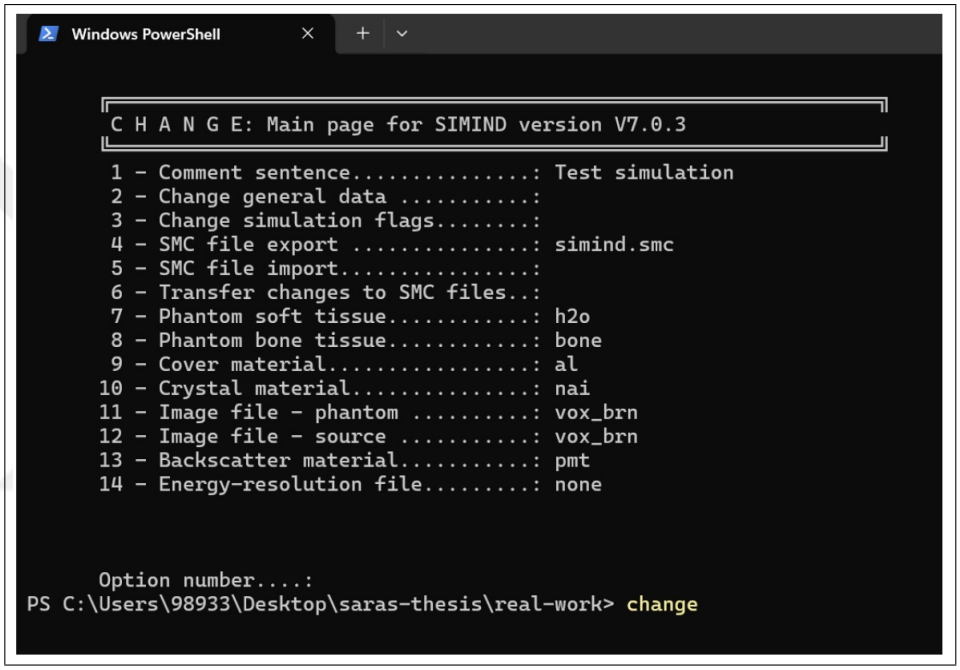

Figure 3.2 The main menu for changing the parameters of the simulation, such as the phantom materials, image files, and other setup options for SPECT simulations.

3.1.3.1 The Monte Carlo simulation process.

The physical processes involved in SPECT imaging are simulated by the Monte Carlo method using random sampling. Within the framework of this project, this includes observing the interactions of gamma photons with tissues and, in the end, modeling how the gamma camera detects them when they are emitted from an anthropomorphic digital brain phantom (like the Zubal phantom). This method aids in enhancing image reconstruction, grasping the distribution of detected photons, and maximizing the efficiency of the imaging system [44],[45].

- **Application in SIMIND**

  In this study, the gamma camera response to the radiotracer distribution within the Zubal phantom is modeled using the SIMIND Monte Carlo simulation software. With SIMIND, we can model a number of parameters, including the detector's energy resolution, the effects of alternative collimator designs (like LEHR), and the influence of photon scattering in various tissues. We may optimize the imaging system for more precise quantification of radiotracer uptake, especially in difficult areas like the parietal and temporal lobes, by changing these simulation settings [8],[16],[32].

3.1.3.2 Imaging system modeling for Monte Carlo simulation.

Table 3.1
Crystal Parameters [3],[4].

Parameters	Camera A manufacturer	Camera B manufacturer	My Values for A and B
Crystal Half-length/Radius (cm)	27	26.65	29
Crystal Thickness (cm)	0.95	0.96	0.95
Crystal Half-width (cm)	20	19.35	22

Table 3.2
Collimator LEHR Properties [3],[4] (* These values are calculated after configuring the parameters in each device.).

Properties	Camera A	Camera B
Hole Shape	Hex	Hex
Number of Holes	86300	148000
Hole Length (cm)	0.2079	0.1282
Hole Diameter (cm)	0.18	0.111
Collimator thickness (cm)	4	2.405
Sensitivity* ($cpm/\mu Ci$)	75.7768*	82.8895*
System Resolution*	6.3*	10.43*

3.2 Simulation setup and data processing

The project's data processing techniques and simulation setup are explained in this section. The main goal is to set up the Anthropomorphic Digital Brain Phantom (Zubal) to accurately replicate I-123 SPECT imaging using the SIMIND Monte Carlo simulation software. Reconstructing the SPECT images and optimizing the simulation settings are two steps in the data processing workflow [8].

3.2.1 SIMIND setup

For I-123 SPECT imaging, the photon transport and detector response are modeled using the Monte Carlo simulation tool SIMIND. The configuration involves setting the geometries of the source, phantom, and detector as well as the necessary physics parameters.

3.2.1.1 Configurations.

Source and Phantom Definition:

- Isotope: Because of its suitable half-life and photon energy for brain imaging, I-123 is used as the radiotracer. As input the simulation receives the photon energy spectrum of I-123, which includes the primary energy peak at 159 keV.
- Phantom: To create anatomically correct depictions of the human brain, the Zubal brain phantom is utilized. In SIMIND, the phantom's voxel size, tissue type, and density are set up to resemble the physical properties of the real brain [7],[22].

Detector configuration:

- Collimator: Because it integrates well with I-123 to produce high-resolution im-

ages, a Low Energy High Resolution (LEHR) collimator is chosen.

- Crystal Properties: The thickness of the NaI(Tl) scintillation crystal is appropriately modeled, matching the features of the simulated gamma camera (e.g., A or B) [3].
- Energy Window: To collect most of the main photons while reducing scatter, the energy window is chosen around the primary energy peak of I-123, usually at ±10% about 159 keV (143 keV–175 keV) [3].

3.2.1.2 Optimization parameters.

The following parameters were particularly adjusted to the brain imaging needs of I-123 SPECT with a LEHR collimator in order to balance resolution, sensitivity, and quantitative accuracy in the SIMIND Monte Carlo simulation. The parameters have been adjusted to provide accurate quantification while minimizing error and keeping sufficient image contrast.

The resolution, sensitivity, and quantitative accuracy of the imaging process have all been carefully balanced for these optimal parameters. The goal of the simulation setup modifications is to produce high-quality SPECT images appropriate for precise quantification and analysis in neurological research utilizing the Zubal brain phantom and I-123 [8],[28],[29].

Crystal dimensions:

- Index 8: Crystal Half-Length/Radius (29 cm): To maximize the detection area and allow for a balance between the field of view and the resolution, the crystal half-length was adjusted to 29 cm. By making this modification, the crystal size will be just right to capture pertinent photon interactions without sacrificing spatial resolution.
- Index 10: Crystal Half-Width (22 cm): By configuring the crystal half-width at 22 cm, an ideal balance between coverage and resolution was achieved. In order to

guarantee that the detection area sufficiently encompasses the brain region while preserving the required resolution for precise imaging, this width was selected [28],[29],[46].

Backscattering material:

- Index 11: Thickness of Backscattering Material (4 cm): The backscattering material's thickness was decreased from 6.6 cm–the manufacturer's recommended value–to 4 cm. This reduction can increase quantification accuracy and contrast in images by reducing the number of scattered photons observed. Because less scatter is seen, this could also result in a minor underestimating of the activity concentration in some areas. Additionally, there is a trade-off taken into consideration in this setup: although this change can enhance image contrast, it may also diminish total signal and sensitivity [47].

Detector position:

- Index 12: Height to Detector Surface (25 cm): A 25-centimeter distance was added between the phantom and the detector surface. This modification was done when using I-123 as the isotope with a LEHR collimator in order to achieve a compromise between resolution and sensitivity. The device achieves enhanced sensitivity by raising the detector height, but at a little resolution trade-off that is controlled to maximize the overall quality of the image [28],[29].

Energy and intrinsic resolution:

- Index 22: Energy Resolution (9%): The energy resolution was changed to 9%, which is a little less than the previous resolution. Although the sensitivity was decreased as a result of this modification, the error rate dropped to 1.3%. This

fine-tuning is necessary to minimize noise and provide dependable primary photon detection by striking the ideal balance between resolution and quantification accuracy.

- Index 23: 0.25 cm Intrinsic Resolution: intrinsic resolution demonstrates the system's basic ability to discriminate between events that are narrowly spaced apart. This resolution is especially important in brain imaging where minute anatomical features are of importance, in order to retain high spatial accuracy in the reconstructed images. The manufacturer value was 0.38 cm for both cameras [28],[29],[33].

Photon histories:

- Index 26: Number of Photon Histories (100 million): To make sure the dataset was statistically strong; the simulation was performed using 100 million photon histories. This huge number of histories is required, especially due to the complexity of brain imaging with I-123, to reduce statistical noise and obtain meaningful quantification [6]. In a similar study that was discussed in literature review, this value assumed to be 4 million.

Cerebellum as a Reference: The cerebellum is often used as a reference region in SPECT studies due to its relatively stable uptake of I-123, which remains unaffected by dopaminergic degeneration.

Cerebellum vol: $130cm^3$ [4]

Index45: 77 (cerebellum code) [42]

Time per projection: 20 s [48]

Source activity: 104 MBq [8],[29]

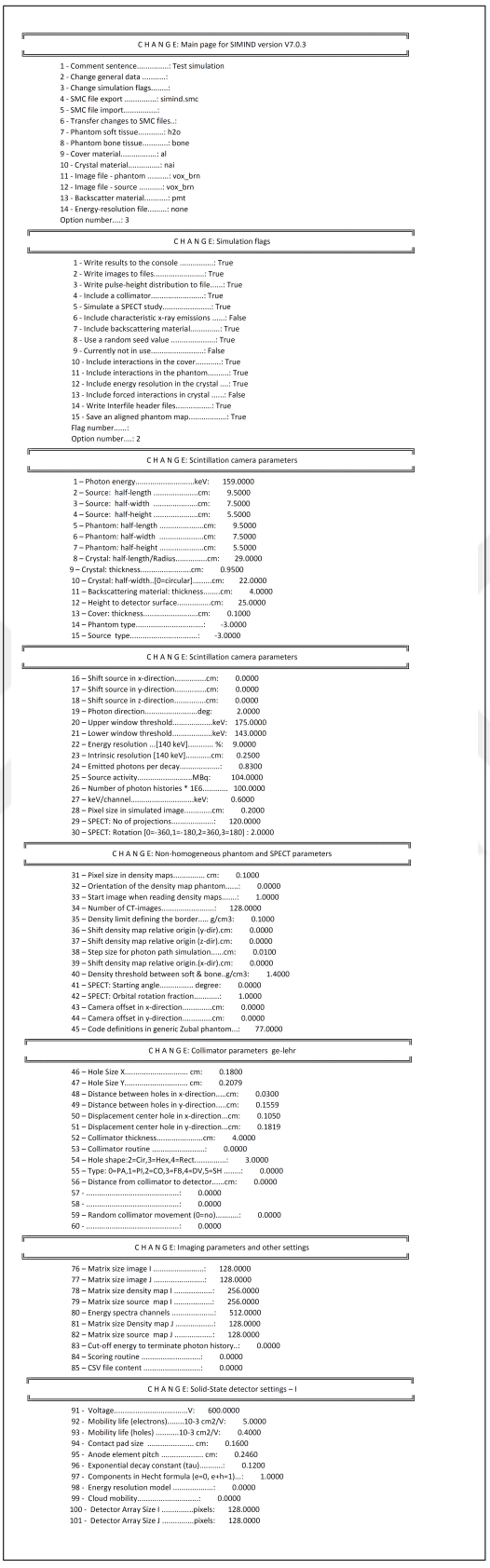

Figure 3.3 Camera A (LEHR)_Cerebellum

Simulation for cerebellum is given in the appendix A.1.

PS C:\$Users$ >simind simind gelehrbrain39/fi:i123/fz:phantom

CALCULATED DETECTOR PARAMETERS

Sensitivity Cpm/uCi: 75.7768

LEHR (Low Energy High Resolution) collimators prioritize resolution over sensitivity.

Higher energy resolution can reduce sensitivity due to tighter constraints on accepted photon energies.

3.2.1.3 Data reconstruction.

Reconstruction Algorithm:

- For image reconstruction in SPECT imaging, an iterative approach called OSEM (Ordered Subsets Expectation Maximization) is utilized. It is a better algorithm than the conventional Expectation Maximization (EM) method, which aims to shorten computing times and accelerate convergence. In contrast to more conventional techniques like filtered back projection, the (OSEM) algorithm produces high-quality images with an enhanced signal-to-noise ratio, which is why it is used for image reconstruction [49].

Iteration Number and Subsets:

- The OSEM method optimizes the number of subsets and iterations to trade between processing time and image quality. The projection data is divided into subsets. Every subset represents part of all the data that was obtained through-

out the scan. The projected estimate and the actual measured data for every subset are compared by the algorithm iteratively updating the image estimate. Generally, depending on the particular imaging needs and the characteristics of the I-123 radiotracer, 8 subsets and 8 and 16 iterations are used. 32 iterations and 15 subsets, made the image quality worse.

Correction Techniques:

- Attenuation Correction: To account for the different densities of brain tissues, attenuation correction is conducted during reconstruction using an attenuation map.
- Scatter Correction: By lowering the contribution of scattered photons the corresponding flags were set to consider for the scatter correction, which increases quantification accuracy.

Quantitative Analysis:

- The radiotracer uptake in certain areas of interest (ROIs), such as the cerebellum, temporal lobe, and parietal lobe, is measured after reconstruction using the SPECT images that have been produced by VINCCI. To verify the correctness of the simulation, the activity concentration in each ROI is computed and compared to known values [6],[12].

Optimization of Image Quality:

- OSEM plays a vital role in guaranteeing that the reconstructed images have high spatial resolution while minimizing noise, which is essential for proper analysis in neurological studies, given our focus on optimizing parameters for resolution

and sensitivity.

$$f_F^{1^x+1}$$

A simplified representation of the OSEM algorithm is:

$$f_j^{(k+1)} = f_j^{(k)} \cdot \sum_{i=1}^{M} \frac{P_{ij} \cdot \frac{y_i}{\sum_{j'} f_{j'}^{(k)}}}{\sum_{M=1}^{N} P_{mj}} \tag{3.1}$$

$f_j^{(k+1)}$ = the updated estimate of the image at voxel j after iteration $k+1$

P_{ij} = the probability that a photon emitted from voxel j is detected by detector i

y_i = the measured projection data for detector i

N and M represent the total number of voxels and detectors, respectively [50]

Reconstruction (OSEM) is given in appendix A.2.

PS C:\$Users$ > smc2castor gelehrbrain39.h00 gelehrbrain3916/ru/at/it:16/su:8/mb:5.2/sm:5

/MB: Activity in the phantom

/SM: Smoothing with filter

True activity concentration: 0.04 MBq/cc (standard value for brain studies)

Mean= measured activity concentration= 0.03939

Standard deviation= 0.006134

$$\text{Quantification error}\% = \frac{|\text{true activity} - \text{measured activity}|}{\text{true activity}}\% = 1.5\% \quad [51] \tag{3.2}$$

$$\text{Signal-to-noise ratio (SNR)} = \frac{Mean}{Std} = 6.4 \quad acceptable \quad [13] \tag{3.3}$$

3.2.1.4 Segmentation.

This project uses Multi-Atlas-based Segmentation [48] to precisely define regions of interest, including the cerebellum and several brain lobes. I was able to segment these regions consistently across simulations by mapping a standard brain atlas to the Zubal phantom. This allowed for precise assessment of radiotracer uptake in certain anatomical areas.

This approach ensures that this research is reproducible and anatomically anchored, especially when comparing the efficacy of different gamma cameras or assessing how different imaging parameters affect quantification accuracy.

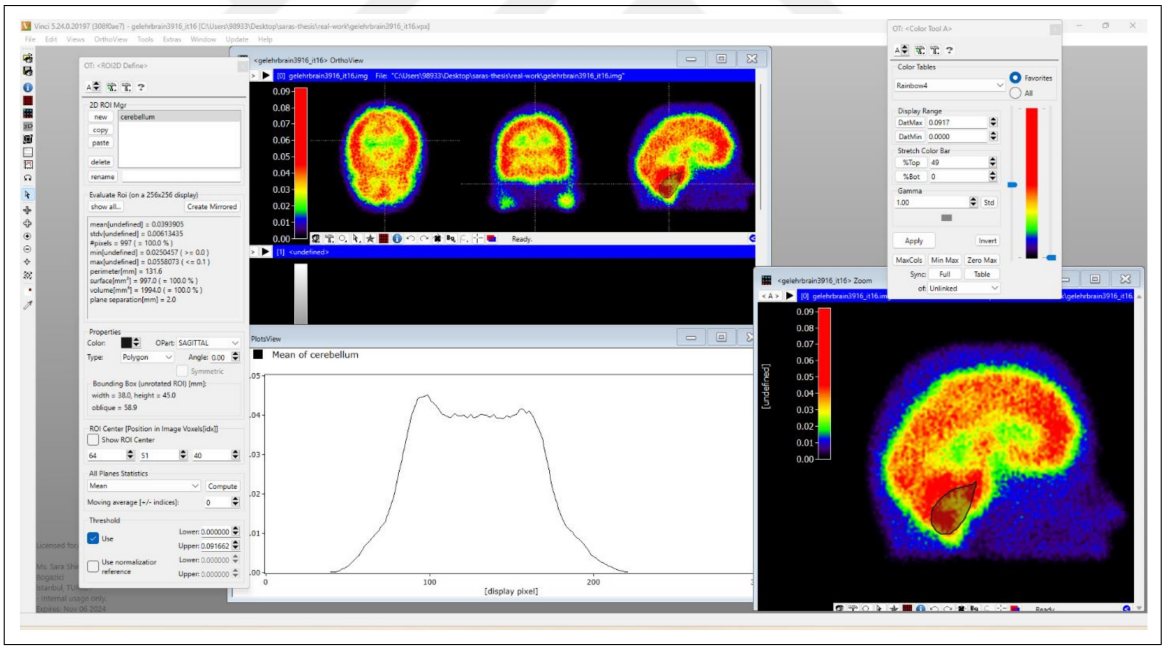

Figure 3.4 The reconstructed brain image for camera A is shown in three views (transaxial, coronal, sagittal). The sagittal view highlights the cerebellum. The accompanying table presents the mean and standard deviation for approximately 1000 pixels in the cerebellum, reflecting the scale's precision by the mean.

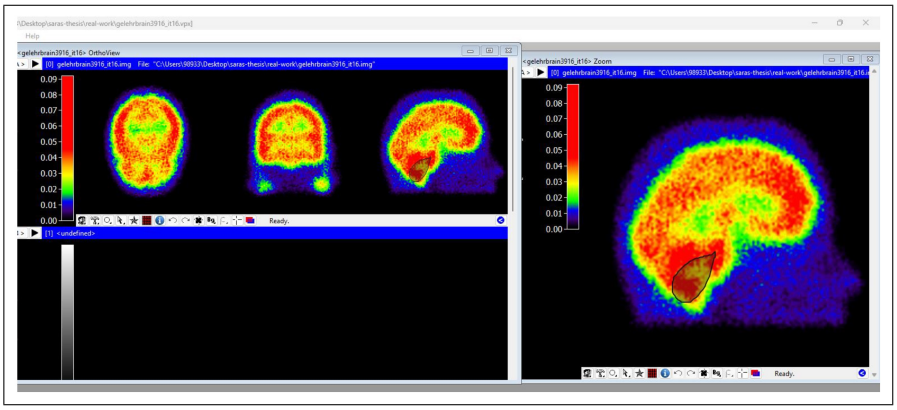

Figure 3.5 Cerebellum sagittal view of camera A

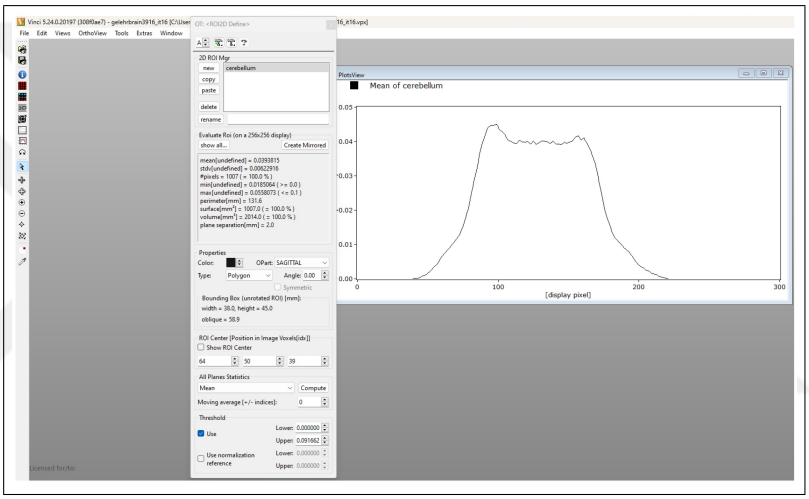

Figure 3.6 Mean and standard deviation of cerebellum for camera A. The precision of the scale can be represented by giving the mean.

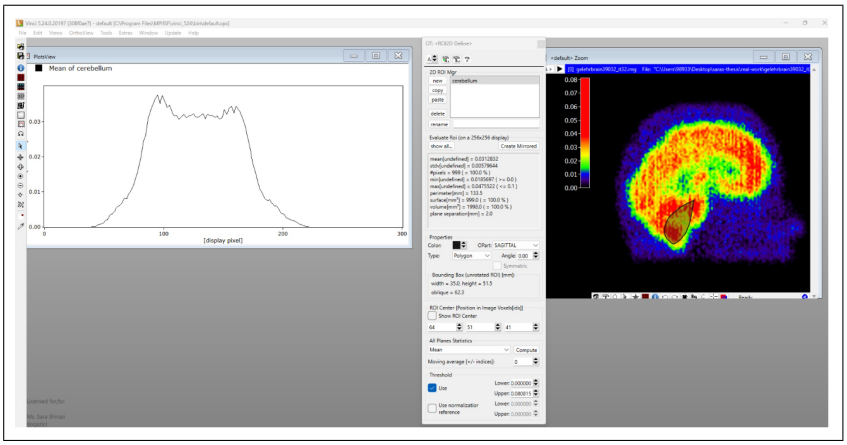

Figure 3.7 Shows cerebellum sagittal view of camera A and also mean and standard deviation, without scatter correction. The precision of the scale can be represented by the mean.

Temporal Lobes: Important for speech and memory, damage here can cause aphasia and memory loss. The medial temporal lobe, including the hippocampus and amygdala, is crucial for memory and emotional regulation. One of the earliest brain regions to exhibit decreased absorption of radiotracer in Alzheimer's disease is the temporal lobe, particularly the hippocampus [18],[52].

Temporal lobes vol: $143cm^3$ [53]

Index45: 114 (temporal lobe code)

At: Time per projection: 20 s

Source activity: 114

CALCULATED DETECTOR PARAMETERS

Sensitivity Cpm/uCi: 75.7822

True activity concentration: 0.04 MBq/cc (standard value for brain studies)

Mean= measured activity concentration= 0.0416327

Standard deviation= 0.009

Quantification error $\% = \frac{|\text{true activity} - \text{measured activity}|}{\text{true activity}}\% = 4\%$

Signal-to-noise ratio (SNR) $= \frac{Mean}{Std} = 4.6$ acceptable

Parietal lobes: The parietal lobes are involved in integrating sensory information and play a role in higher cognitive functions such as attention and perception.

The later stages of Alzheimer's disease involve involvement of the parietal lobe.

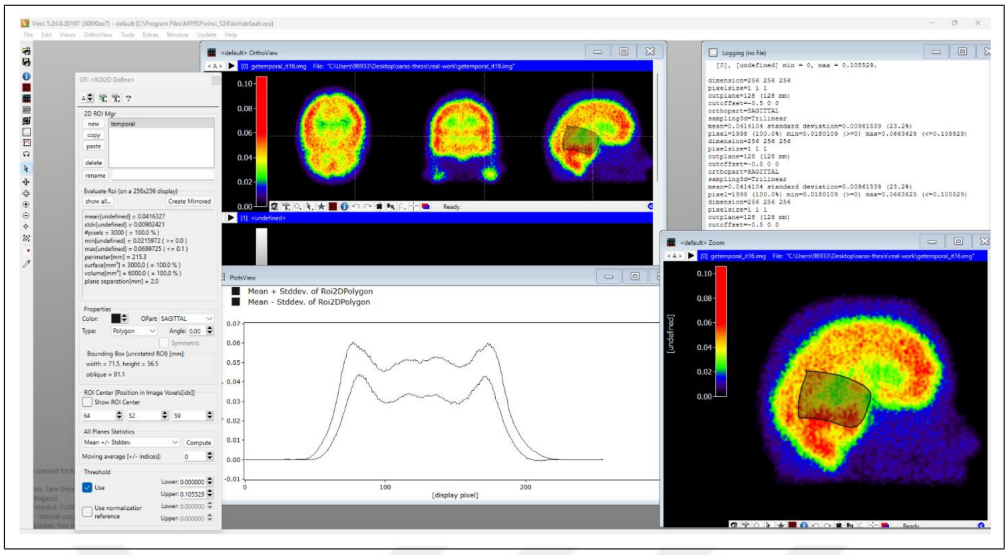

Figure 3.8 The reconstructed brain image for camera A is shown in three views (transaxial, coronal, sagittal). The sagittal view highlights the temporal lobe. A table on the left displays the mean and standard deviation for approximately 3000 pixels in the temporal lobe, with precision indicated by the mean ± standard deviation.

More advanced cognitive deterioration is correlated with decreased uptake in this domain.

Parietal lobes vol: $150cm^3$ [54]

Index45: 117 (parietal lobe code)

Time per projection: 20 s

Source activity: 120

CALCULATED DETECTOR PARAMETERS

Sensitivity Cpm/uCi: 75.7865

True activity concentration: 0.04 MBq/cc (standard value for brain studies)

Mean= measured activity concentration= 0.043

Standard deviation= 0.011

Quantification error % $= \frac{|\text{true activity} - \text{measured activity}|}{\text{true activity}} \% = 7.5\%$

Signal-to-noise ratio (SNR) $= \frac{Mean}{Std} = 3.9$ acceptable

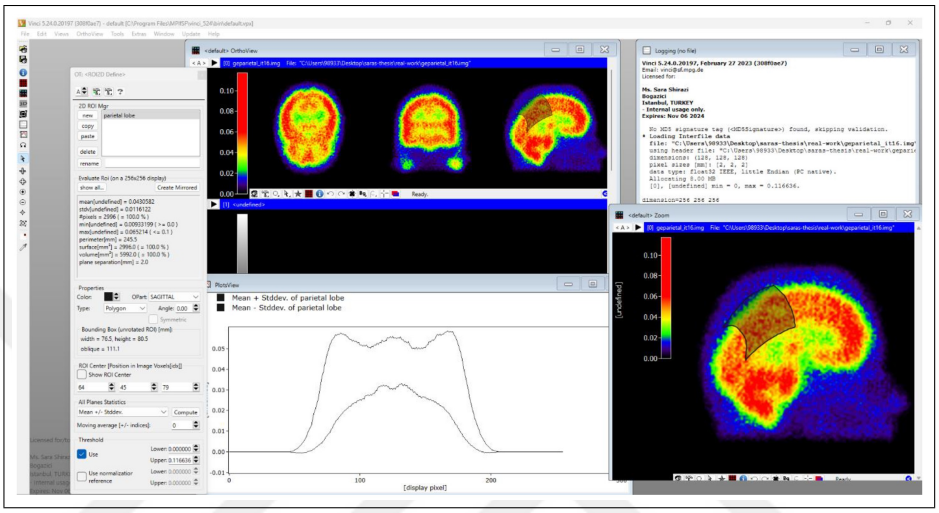

Figure 3.9 The reconstructed brain image for camera A is displayed in three views, with the sagittal view highlighting the parietal lobe. The left table shows the mean and standard deviation for 3000 pixels in the parietal lobe.

The overall system resolution can be estimated using the formula:

$$R_{sys} = \sqrt{R^2_{intrinsic} + R^2_{collimator}} \quad [20] \tag{3.4}$$

Intrinsic Resolution: 0.25 cm

The collimator resolution can be approximated using:

$$R_{collimator} = \frac{\text{Hole size}}{\sqrt{12}} + \frac{\text{Distance}}{\text{Septal thickness}} \tag{3.5}$$

Using the values from the configuration:

- Hole Size (X): 0.18 cm
- Collimator Thickness: 4 cm

$$R_{collimator} = \frac{0.18}{\sqrt{12}} + \frac{25}{4}$$

$$R_{collimator} = 6.3$$

$$R_{sys}^2 = 0.25^2 + 6.3^2 = 39.7771$$

$$R_{sys} = 6.3$$

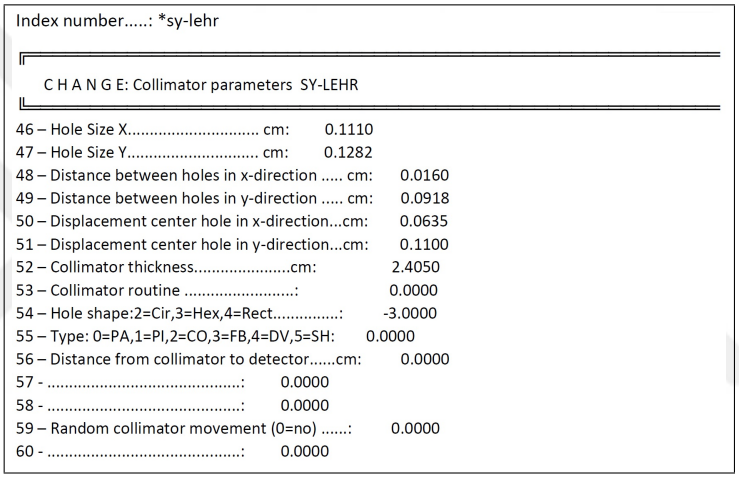

Figure 3.10 Camera B (Cerebellum)

All the parameters are same as camera A. Only difference is that I changed the camera to B and LEHR collimator values changed accordingly.

Simulation for cerebellum

PS C:\$Users$ >simind simind sylehrbrain39/fi:i123/fz:phantom

CALCULATED DETECTOR PARAMETERS

Sensitivity Cpm/uCi: 82.8895

Reconstruction (OSEM)

PS C:\$Users$ > smc2castor sylehrbrain39.h00 sylehrbrain3916/ru/at/it:16/su:8/mb:5.2/sm:5

The reconstruction OSEM algorithm results with 16 iterations and 8 subsets

True activity concentration: 0.04 MBq/cc (standard value for brain studies)

Mean= measured activity concentration= 0.0413961

Standard deviation= 0.0083

Quantification error % $= \frac{|\text{true activity} - \text{measured activity}|}{\text{true activity}} \% = 3.5\%$

Signal-to-noise ratio (SNR) $= \frac{Mean}{Std} = 5$ acceptable

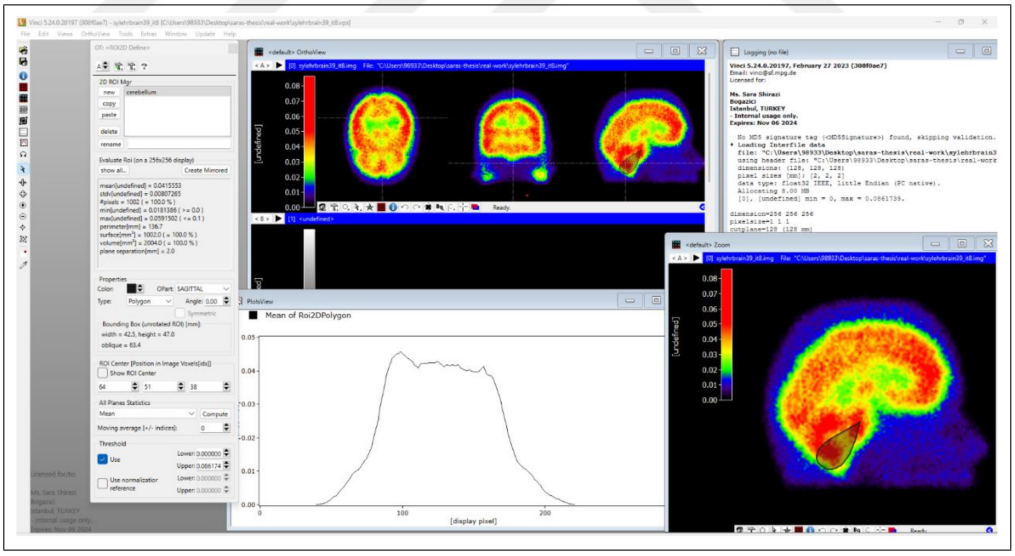

Figure 3.11 The reconstructed brain image for camera B is shown in three views, with the sagittal view highlighting the cerebellum. The left table shows the mean and standard deviation for 1000 pixels in the cerebellum.

Simulation for temporal lobe

PS C:\$Users$ >simind simind sytemporal/fi:i123/fz:phantom

CALCULATED DETECTOR PARAMETERS

Sensitivity Cpm/uCi: 82.8862

Reconstruction (OSEM)

PS C:\$Users$ > smc2castor sytemporal.h00 sytemporal/ru/at/it:16/su:8/mb:5.7/sm:5

The reconstruction OSEM algorithm results with 16 iterations and 8 subsets

True activity concentration: 0.04 MBq/cc (standard value for brain studies)

Mean= measured activity concentration= 0.0424

Standard deviation= 0.01

Quantification error % = $\frac{|\text{true activity} - \text{measured activity}|}{\text{true activity}}\% = 6\%$

Signal-to-noise ratio (SNR) = $\frac{Mean}{Std} = 3.8$ acceptable

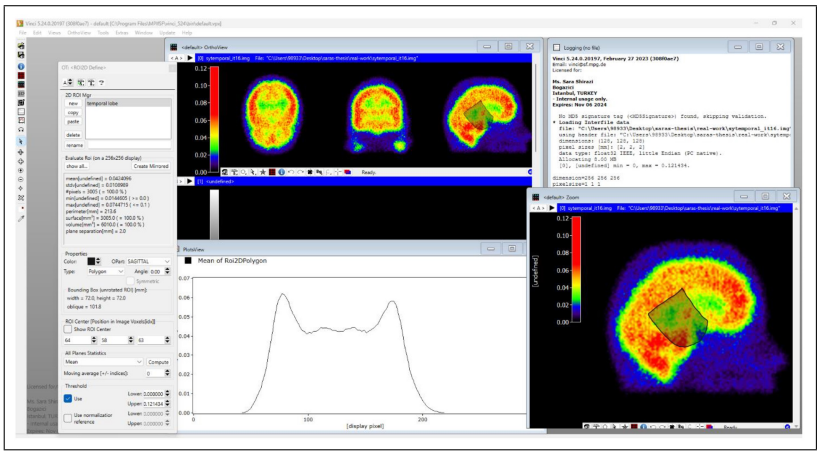

Figure 3.12 The reconstructed brain image for camera B is shown in three views, with the sagittal view highlighting the temporal lobe. The left table shows the mean and standard deviation for 3000 pixels in the temporal lobe.

Simulation for parietal lobe

PS C:\$Users$ >simind simind syparietal/fi:i123/fz:phantom

CALCULATED DETECTOR PARAMETERS

Sensitivity Cpm/uCi: 82.8768

Reconstruction (OSEM)

PS C:\$Users$ > smc2castor syparietal.h00 syparietal/ru/at/it:16/su:8/mb:6/sm:5

The reconstruction OSEM algorithm results with 16 iterations and 8 subsets

True activity concentration: 0.04 MBq/cc (standard value for brain studies)

Mean= measured activity concentration= 0.0456

Standard deviation= 0.014

Quantification error % = $\frac{|\text{true activity} - \text{measured activity}|}{\text{true activity}}\% = 12\%$

Signal-to-noise ratio (SNR) = $\frac{Mean}{Std} = 3.2$ acceptable

Compared to other brain regions, measuring uptake in the parietal lobe can be more difficult.

Because of its variable thickness and the existence of sulci and gyri, the parietal lobe is especially exposed to the partial volume effect (PVE), which poses a serious problem for brain imaging. PVE can lead to inaccurate uptake quantification by underestimating activity in thin structures and overestimating it in thicker areas [34].

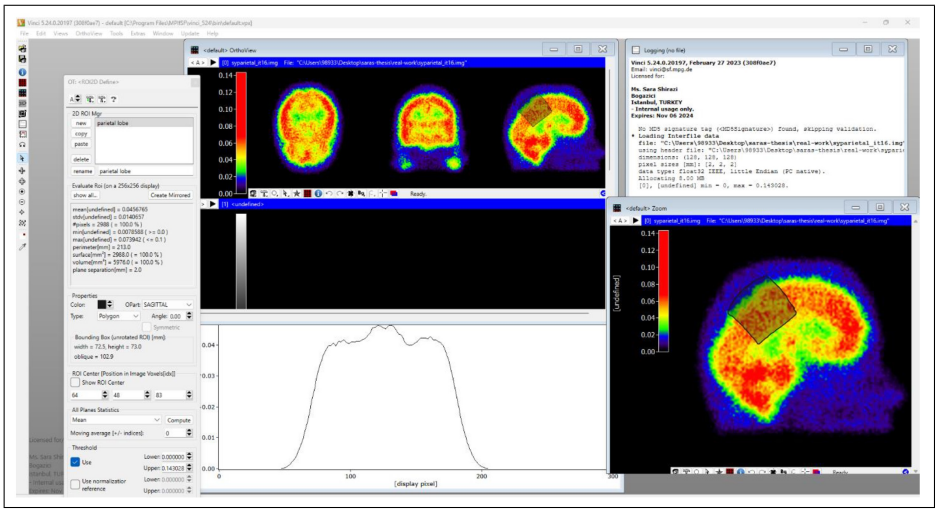

Figure 3.13 The reconstructed brain image for camera B is shown in three views, with the sagittal view highlighting the parietal lobe. The left table shows the mean and standard deviation for 3000 pixels in the parietal lobe.

The overall system resolution can be estimated using the formula:

$$R_{sys} = \sqrt{R_{intrinsic}^2 + R_{collimator}^2} \quad [20]$$

Intrinsic Resolution: 0.25 cm

The collimator resolution can be approximated using:

$$R_{collimator} = \frac{\text{Hole size}}{\sqrt{12}} + \frac{\text{Distance}}{\text{Septal thickness}}$$

Using the values from the configuration:

- Hole Size (X): 0.111cm
- Collimator Thickness: 2.405 cm

$$R_{collimator} = \frac{0.111}{\sqrt{12}} + \frac{25}{2.405}$$

$$R_{collimator} = 10.427$$

$$R_{sys}^2 = 0.25^2 + 10.427^2$$

$$R_{sys} = 10.43$$

3.3 Analysis methods

The project's methods of analysis focus on analyzing the quantitative measurements given by the VINCCI program, which is utilized to analyze the SPECT images that have been reconstructed. Understanding the distribution and variability of radiotracer absorption in the relevant brain regions requires a knowledge of these measurements, particularly the mean activity concentration and standard deviation.

3.3.1 Mean activity concentration

In this research, the VINCCI software automatically determines the mean activity concentration while reconstructing the image. This measure shows an average uptake of radiotracer in a designated brain region of interest (ROI), such as the parietal lobe, temporal lobe, and cerebellum [10],[55].

- Biological Activity Indicator: Within the ROI, the mean activity concentration represents the amount of biological or functional activity. Greater value indicates higher radiotracer uptake, which may signify increased metabolic or functional activity in that area.
- Comparing Different Systems: This metric enables the comparison of radiotracer uptake quantification between two distinct gamma camera systems (A and B) under similar physical settings, assisting in the assessment of each system's reliability and accuracy. (The only difference between these two systems is the LEHR collimator parameter values, which are different according to each system design.)

- Diagnostic insight: Offers information about the physiological condition of the brain's tissues, making it easier identify anomalies or changes in activity that could be related to neurological disorders.

- System Performance Evaluation: By assessing the accuracy and consistency of the quantified uptake, it enables a direct comparison of imaging performance across various configurations and systems [9].

The average amount of radiotracer uptake within particular brain regions is directly reflected in the mean activity concentration in this project. Determining the efficacy of the gamma cameras in measuring and representing biological activity is critical for the diagnosis of diseases such as Parkinson's and Alzheimer's. The standard deviation shows the consistency of the radiotracer uptake within the ROI. It highlights how uniform or variable the uptake is across the region. In your project, this metric is essential for evaluating the precision of the imaging and reconstruction process, identifying potential issues with image quality, and ensuring that the quantified values are reliable and accurate. The means obtained are relatively close to the actual activity concentration, as the findings show [6],[56].

3.3.2 Standard deviation

Via the VINCCI program, the standard deviation of the activity concentration quantifies the variability or dispersion of the radiotracer uptake values inside the ROI.

- Measure of Variability: The standard deviation shows how much the ROI's radiotracer uptake varies from one measurement to the next. A low standard deviation denotes homogeneity within the region since it shows that the uptake values are near to the mean. On the other hand, a high standard deviation denotes increased variability and may be indicative of noise, artifacts, or irregular uptake patterns.

- Impact on Quantification Accuracy: The standard deviation is helpful for evaluating the gamma camera precision and image reconstruction process efficacy. Considerable variations could indicate problems with noise, partial volume effects, or image resolution.

- Quantification Reliability: To understand the dependability of the quantification process, one must evaluate the standard deviation. Reduced variability indicates more exact and accurate quantification, which is essential for making diagnoses.

- Quality Control: The study can evaluate the quality of the reconstructed images and make sure that the imaging procedure yields consistent and trustworthy data via analysis of the standard deviation [45].

The ROI's radiotracer uptake is consistently displayed by the standard deviation. It draws attention to how consistent or inconsistent the uptake is throughout the area. This measure is crucial to this project since it will let us assess how precisely the imaging and reconstruction process worked, identify any possible image quality problems, and make sure the quantified values are accurate and dependable. My results' low standard deviation demonstrates the great dependability of this work [6].

4. RESULTS

4.1 Camera A and B results

A and B Gamma Cameras Phantom Simulation output file for LEHR Collimator

Table 4.1
Cerebellum (EXP NO: experiment number, IT NO: iteration number, SC: with and without scatter correction, QE: quantification error, SNR: signal to noise ratio)

EXP.NO	TRACER	DEVICE	IT.NO	SUBSET NO	SC	QE
1	I-123	Camera A	8	8	+	2%
2	I-123	Camera A	8	8	-	21.5%
3	I-123	Camera A	16	8	+	1.5%
4	I-123	Camera A	16	8	-	20%
5	I-123	Camera A	32	15	+	3%
6	I-123	Camera A	32	15	-	22%
7	I-123	Camera B	8	8	+	3.8%
8	I-123	Camera B	8	8	-	12.5%
9	I-123	Camera B	16	8	+	3.5%
10	I-123	Camera B	16	8	-	11.5%
11	I-123	Camera B	32	15	+	4%
12	I-123	Camera B	32	15	-	13.8%

Table 4.2
Temporal lobe

EXP.NO	TRACER	DEVICE	IT.NO	SUBSET NO	SC	QE
1	I-123	Camera A	8	8	+	3.3%
2	I-123	Camera A	8	8	-	27%
3	I-123	Camera A	16	8	+	3.1%
4	I-123	Camera A	16	8	-	26%
5	I-123	Camera B	8	8	+	8.3%
6	I-123	Camera B	8	8	-	25%

7	I-123	Camera B	16	8	+	6%
8	I-123	Camera B	16	8	-	22%

Table 4.3
Parietal lobe

EXP.NO	TRACER	DEVICE	IT.NO	SUBSET NO	SC	QE
1	I-123	Camera A	8	8	+	8.8%
3	I-123	Camera A	16	8	+	7.5%
5	I-123	Camera B	8	8	+	16%
7	I-123	Camera B	16	8	+	12%

4.2 Recovery coefficient (RC)

To evaluate the absolute quantification of different SPECT systems, RC determined. RC was defined as the ratio of the measured activity concentration (a) and the true activity concentration (A)

$$RC = a/A \tag{4.1}$$

RC provides insight into how accurately the SPECT system can quantify radiotracer uptake in a specific region. It is used to correct for partial volume effects, which can cause underestimation of activity concentrations in small structures [27].

The Recovery Coefficient is typically calculated as follows:

$$RC = \frac{\text{Measured Activity Concentration } \left(\frac{MBq}{ml}\right)}{\text{True Activity Concentration } \left(\frac{MBq}{ml}\right)} \tag{4.2}$$

Compute RC for Each ROI:

For each region, calculate the RC using the formula provided. The closer the RC is to 1, the more accurate the quantification.

Camera A:

$$R_{cerebellum} = \frac{0.03919}{0.04} = 0.98$$

$$R_{temporal} = \frac{0.0416327}{0.04} = 1.04$$

$$R_{parietal} = \frac{0.043}{0.04} = 1.07$$

Camera B:

$$R_{cerebellum} = \frac{0.0413961}{0.04} = 1.03$$

$$R_{temporal} = \frac{0.0424}{0.04} = 1.06$$

$$R_{parietal} = \frac{0.0456}{0.04} = 1.14$$

Table 4.4
Recovery Coefficient

Region	Camera A	Camera B
Cerebellum	0.98	1.03
Temporal lobe	1.04	1.06
Parietal lobe	1.07	1.14

5. DISCUSSION

The quantification error I got for cameras A and B was comparatively the same but according to the different values for LEHR collimator parameters in these two cameras, there was slightly difference in sensitivity and system resolution in each device. Also, there were some preferred manufacturer differences in some other parameters of the Gamma camera in both devices like the distance from the origin to the detector surface, the detector thickness, also the crystal sizes and ..., so was resulting in different acquisition time and cost of manufacturing the device and so many other parameters. All the parameters were as the same for two devices rather than the collimator settings. There would still be inherent differences between the two systems due to their underlying technologies and design philosophies. These differences include:

- **Technology**

  Detectors:

  - Camera A: Usually use detectors that are based on sodium iodide doped with thallium, or NaI(Tl). These detectors are famous for having good resolution and high sensitivity.
  - Camera B: These devices also use NaI(Tl) detectors, but their setups may differ due to differences in photomultiplier tubes (PMTs) or electronics, which may have an impact on how well they work.

  Electronics and Signal Processing:

  - Image quality, noise reduction, and sensitivity can be affected by the unique electronics and algorithms used by each manufacturer for signal processing.

  Collimator Design and Manufacturing:

  - Cameras A and B may differ in terms of manufacturing precision and design tolerances, even when the collimators have the same size and materials. This could have an impact on the collimator's overall performance.

LEHR Collimator:

- Camera A: LEHR collimators feature particular designs to reduce scatter and enhance resolution, and they are optimized for the I-123 isotope.
- Camera B: Also provides LEHR collimators, although there may be variations in hole size, shape, and septal thickness that affect performance and sensitivity.

Software and System Calibration:

- Every manufacturer has their own software algorithms and calibration processes for image enhancement, correction, and reconstruction. Both the final image quality and quantitative accuracy may be impacted by these.

Build Quality and Mechanical Design:

- Variations in the gantry and detector movement mechanisms' mechanical designs and build quality can result in differences in dependability and simplicity of use.

User Interface and Workflow:

- The manufacturer customizes the user interface and workflow for each system, which may have an impact on how simple and effective it is to use in clinical settings.

Because of these intrinsic differences, A and B gamma cameras may differ in terms of overall performance, image quality, and user experience even in cases where the physical parameters are the same [2],[19],[46].

Camera A:

- According to the camera A brochure, the Extended Low Energy General Purpose ELEGP collimator is frequently advised for I-123 imaging. I adjusted a few more camera settings to employ the LEHR collimator, maintain the lowest possible error, and achieve an appropriate balance between sensitivity and resolution.

- Improved magnification imaging is possible with the optional Fan Beam collimator, which is very helpful for brain research. SIMIND does not supply the fan beam collimator options. Using a parallel hole collimator (LEHR) was the goal of my project [28].

Camera B:

- Suggested Collimator: For I-123, camera B frequently use LEHR (Low Energy High Resolution) collimators.
- Technology: It is appropriate for in-depth research such as brain imaging using I-123 since it also makes use of NaI(Tl) detectors that are optimized for high-resolution imaging [29].

Why LEHR?

- The Low Energy High Resolution (LEHR) collimator is usually a good choice for I-123 brain imaging. These are a few reasons for why:
    1. Energy Range: The energy at which I-123 emits gamma rays is around 159 keV. Low-energy photons are effectively handled by LEHR collimators.
- Resolution: Higher resolution images are produced by LEHR collimators, which is essential for precise localization of activity in detailed brain imaging [57].
- Sensitivity: Despite having a lower sensitivity than Low Energy General Purpose (LEGP) collimators, LEHR collimators are nevertheless preferred for diagnostic brain imaging because of their superior resolution, which is essential for capturing anatomical detail [6],[25],[58].

High Resolution Requirement:

- Because LEHR collimators may offer the resolution required for detailed brain imaging which is essential for detecting small or subtle changes in the structure or function of the brain they are frequently used.

Why is high resolution important?

- Accurately localizing the I-123 uptake within certain lobes and distinguishing between closely spaced brain regions require high spatial resolution.
- Accurate assessment and clear visualization of minor structures, such as specific lobes or sub-lobar regions, are ensured by good resolution [5],[59].

Factors Affecting Resolution:

- Type of Collimator: High-resolution imaging is frequently achieved with LEHR collimators, which is advantageous for brain research.
- Intrinsic Resolution: Resolving small structures and enhancing spatial detail are possible with lower intrinsic resolution values [6],[7].

Trade-off with Resolution:

- Sensitivity and resolution are typically mutually exclusive. Decreased sensitivity is frequently accompanied with higher resolution, therefore it's critical to balance these depending on your unique imaging objectives.

Table 5.1
New contribution

Properties	Camera A manufacturer	Camera A simulated	Camera B simulated	Camera B manufacturer
Sensitivity ($cpm/\mu Ci$) (100 mm)	160 (Tc99m)	75.7768	82.8895	202 (Tc99m)
Intrinsic spatial resolution (mm)	3.8 mm	2.5 mm	2.5 mm	3.8 mm
Intrinsic energy resolution	9.8	9	9	9.9
System Resolution	7.4	6.3	10.43	13.3

Why I-123?

- Compared to Tc-99m, which has a photon energy of 140 keV, -123 has a photon energy of 159 keV, which is closer to the ideal range for gamma cameras and offers greater image resolution. I-123's slightly higher energy causes less scattering and better penetration, which enhances image quality.

- The half-life of I-123 is approximately 13.2 hours, which is both enough long to enable prolonged imaging and comprehensive radiopharmaceutical distribution, and sufficiently quick to reduce the patient's exposure to radiation. With a half-life of six hours, Tc-99m could not be long enough for some imaging methods that call for longer uptake times.

- I-123's ideal photon energy and decreased scatter amount allow for improved image contrast and resolution in SPECT imaging. In brain imaging, where precise viewing of small structures is required, this can be especially significant [57].

- Tc-99m has been used extensively in clinical practice for a long time, and its usage is supported by established protocols and a wealth of knowledge. Physicians have greater experience with Tc-99m operations, which may have an impact on the isotope selection.

- Tc-99m exposes patients and medical staff to less radiation because of its shorter half-life (6 hours) than that of I-123 (13.2 hours). This may play a big role in

why Tc-99m is preferred, particularly in hectic clinical environments.

- I-123 is still a good option for specialized brain imaging research where precise targeting and excellent resolution are essential [58],[60].

Quantification Accuracy

- Because it directly measures the concentration of the radiotracer (I-123) within various brain lobes, quantification accuracy is very important. Precise measurement enables you to dependably compare the uptake rates in different regions.
- High quantification accuracy means that actual variations in tracer uptake are reflected in the variations in measured activity.

For my study comparing I-123 absorption in different brain lobes, **quantification accuracy** should be my top priority, followed by **resolution** to ensure clear delineation of brain structures [6],[7].

Simulation time

The simulation time of system B was double of system A, due to [8]:

1. Higher Sensitivity and Photon Processing:
    - Increased Photon Interactions: B' increased sensitivity enables the system to detect a greater number of photons. This results in processing more photon interactions in simulations, which can lead to a considerable increase in computation time.
    - Simulation Workload: Longer simulation periods result from the requirement to precisely and more sensitively model each interaction, which necessitates more computational processes.

2. Noise and Correction Algorithms:

    - Scatter and Attenuation Corrections: Increased sensitivity may also result in the detection of more background noise and scatter, requiring more computation to make adjustments.

3. Design of collimator

Scattering in SPECT Imaging

A key factor in determining the accuracy and quality of SPECT imaging data is scattering. I made sure that my models accurately reflected the imaging settings by included scattering, which enhanced quantification, enhanced image quality, and decreased error.

An increasingly precise representation of the activity distribution is possible by incorporating scattering, which enables adjustments that take deflected photons into account [3].

Compton Scattering:

- Mechanism: When a photon collides with an electron in the outer shell, it loses energy and changes direction. This is known as Compton scattering.
- Effect on Images: Inaccurate activity quantification can result from Compton scattering's reduction of spatial resolution and contrast in images.
- By reducing the effect of scattered photons that add to background noise, scattering corrections can enhance image contrast and resolution.
- Detailed scattering models that take scattering effects into account are included in the simulation software (SIMIND) [43].

Limitation

Resolution vs. Sensitivity Trade-off:

- In these systems (A vs. B), the ability to obtain both high-resolution and high-sensitivity images concurrently may be limited by the trade-off between resolution and sensitivity.

Differences in Camera Technologies:

- It is important to properly account for biases introduced by differences in detector technology, signal processing methods, and calibration procedures between A and B systems [28],[29].

Parietal Lobe Challenges:

- It can be more challenging to measure uptake in the parietal lobe than in other parts of the brain. The partial volume effect (PVE) is particularly problematic for brain imaging in the parietal lobe due to its variable thickness and the presence of sulci and gyri. Because PVE underestimates activity in thin structures and overestimates it in thicker sections, it can result in mistaken uptake estimation [34].

Renal Excretion:

- The reliance on renal excretion can be considered a limitation of using I-123, especially in patients with compromised kidney function. However, this limitation can be managed through careful patient selection, dose adjustment, and monitoring. In some cases, alternative imaging agents might be preferred to avoid

potential complications. By understanding these considerations, clinicians can make informed decisions about the use of I-123 in patients with varying levels of kidney function, balancing the need for diagnostic accuracy with patient safety [19].

Future works

1. Compare different collimator types when available by SIMIND [42].
2. Compare different isotopes in same case imaging
    - Innovation: Although I-123 is the main focus, the project may represent a substantial innovation if it involves any part of creating or validating new radiotracers with a particular affinity for novel targets.
3. Consider Additional Imaging Modalities
    - Hybrid Imaging: To take advantage of the anatomical information offered by CT or MRI scans, combine I-123 SPECT pictures with the data if at all possible. This will help to get more precise assessment of brain structure and function [4],[10].
4. Post-Processing for PVE:
    - Take into account PVE post-reconstruction corrections, which could involve modifications based on anatomical information from CT or MRI scans.

6. CONCLUSION

Using I-123 isotope and different (LEHR) collimator values, keeping all other physical parameters same for both systems (I have explored detailed configurations in SIMIND for both A and B systems, optimizing parameters such as scintillation crystal and detector settings, energy resolution), I Conducted a comprehensive comparison across different gamma camera systems (A vs. B) to validate quantification accuracy and identified optimal settings for this specific brain imaging. Comparing A and B gamma cameras found differences in spatial resolution and sensitivity, with camera A system being better suited for detecting small lesions and the camera B providing better overall sensitivity. I implemented advanced image reconstruction algorithm, novel iterations, OSEM that improves image quality, reduces noise, and enhances resolution beyond conventional methods. I got the best result with 16 iterations and 8 subsets. Highlighting these optimizations and how they lead to improved image quality or reduced simulation times is a valuable contribution [61].

My study systematically examines the trade-offs between resolution and sensitivity, especially in comparing different camera systems. It also includes efforts to enhance quantification accuracy. As reported by RC, I evaluated the accuracy of absolute quantification that the SPECT system can use to quantify radiotracer uptake in the cerebellum, temporal, and parietal lobes of the brain. Quantification error for cerebellum in camera A was considerably low: 1.5% and camera B: 3.5%. For temporal lobe in camera A: 3.1% and camera B: 6%. For Parietal lobe in camera A: 7.5 and camera B: 12%, which is acceptable. According to the manufacturer, error generally was around 5% using other combinations like Tc99m or ELEGP collimator in all studies.

It emphasizes how my findings can influence clinical decision-making, particularly in choosing the right equipment and settings for specific diagnostic needs.

Both cameras are suitable for I-123 imaging, but the choice may depend on the

specific requirements of the imaging study.

APPENDIX A. PARAMETERS USED DURING THE STUDY

A.1 Simulation for Cerebellum Camera A

PS C:\$Users$ >simind simind gelehrbrain39/fi:i123/fz:phantom

SIMIND Monte Carlo Simulation Program V7.0.3	
Phantom(S): h2o	Crystal...: nai InputFile.: simind
Phantom(B): bone	BackScatt.: pmt OutputFile: gelehrbrain39
Collimator: pb_sb2	SourceRout: smap SourceFile: vox_brn
Cover.....: al	ScoreRout.: none DensityMap: vox_brn
PhotonEnergy.....: 159	i123 PhotonsPerProj....: 9102759
EnergyResolution...: 9	Matrix Activity.....: 104
MaxScatterOrder....: 3	Spectra DetectorLenght....: 29
DetectorWidth.....: 22	ge-lehr DetectorHeight....: 0.95
UpperEneWindowTresh: 175	SPECT Distance to det...: 25
LowerEneWindowTresh: 143	Bscatt ShiftSource X.....: 0
PixelSize I.....: 0.2	Random ShiftSource Y.....: 0
PixelSize J.....: 0.2	Cover ShiftSource Z.....: 0
HalfLength S.....: 9.5	Phantom HalfLength P.....: 9.5
HalfWidth S.....: 7.5	Resolut HalfWidth P.....: 7.5
HalfHeight S.....: 5.5	Header HalfHeight P.....: 5.5
SourceType.....: ZubalVoxBrn	SaveMap PhantomType.....: ZubalVoxBrn
GENERAL DATA	
keV/channel.....: 0.6	CutoffEnergy.....: 0
Photons/Bq.....: 1.72885	StartingAngle.....: 0
CameraOffset X.....: 0	CoverThickness....: 0.1
CameraOffset Y.....: 0	BackscatterThickn.: 4
MatrixSize I.....: 128	IntrinsicResolut..: 0.25
MatrixSize J.....: 128	AcceptanceAngle...: 2.97456
Emission type.....: 2	Initial Weight....: 19.75234
NN ScalingFactor...: 1	Energy Channels...: 512
SPECT DATA	
RotationMode.....: 360	Nr of Projections.: 120

RotationAngle.....: 3 Projection.[start]: 1

Orbital fraction...: 1 Projection...[end]: 120

COLLIMATOR DATA FOR ROUTINE: Analytical

CollimatorCode.....: ge-lehr CollimatorType....: Parallel

HoleSize X.....: 0.18 Distance X.....: 0.03

HoleSize Y.....: 0.20785 Distance Y.....: 0.1299

CenterShift X.....: 0.105 X-Ray flag.....: F

CenterShift Y.....: 0.18187 CollimThickness...: 4

HoleShape.....: Hexagonal Space Coll2Det....: 0

CollDepValue [56]..: 0 CollDepValue [58].: 0

CollDepValue[59]..: 0 CollDepValue [57].: 0

IMAGE-BASED PHANTOM DATA

RotationCentre.....: 129,129 Bone definition...: 1400

CT-Pixel size.....: 0.1 Slice thickness...: 0.14844

StartImage.....: 1 No of CT-Images...: 128

MatrixSize I.....: 256 CtmapOrientation..: 0

MatrixSize J.....: 256 StepSize.....: 0.01

CenterPoint I.....: 129 ShiftPhantom X....: 0

CenterPoint J.....: 129 ShiftPhantom Y....: 0

CenterPoint K.....: 65 ShiftPhantom Z....: 0

PHANTOM DATA FROM FILE: phantom.zub section: 2

Code Volume	Density	Voxels	Volume(mL)	MBq	MBq/mL	Value
1: skin	1.040	139785	0.207E+03	0.319E+01	0.154E+02	2.000
2: brain	1.040	130250	0.193E+03	0.149E+01	0.770E+01	1.000
3: spinal cord	1.040	1733	0.257E+01	0.396E-01	0.154E+02	2.000
4: skull	1.300	271508	0.403E+03	0.310E+01	0.770E+01	1.000
5: spine	1.300	15832	0.235E+02	0.181E+00	0.770E+01	1.000
9: skeletal muscle	1.040	213325	0.317E+03	0.487E+01	0.154E+02	2.000
15: pharynx	1.040	2707	0.402E+01	0.619E-01	0.154E+02	2.000
22: fat	1.040	31096	0.462E+02	0.355E+00	0.770E+01	1.000
23: blood pool	1.040	14348	0.213E+02	0.328E+00	0.154E+02	2.000
26: bone marrow	1.040	575	0.854E+00	0.131E-01	0.154E+02	2.000
30: cartilage	1.040	30174	0.448E+02	0.345E+00	0.770E+01	1.000
70: dens of axis	1.300	788	0.117E+01	0.900E-02	0.770E+01	1.000
71: jaw bone	1.300	3276	0.486E+01	0.374E-01	0.770E+01	1.000
72: parotid gland	1.040	18522	0.275E+02	0.169E+01	0.616E+02	8.000

74: lacrimal glands	1.040	1488	0.221E+01	0.340E-01	0.154E+02	2.000
75: spinal canal	1.040	4550	0.675E+01	0.520E-01	0.770E+01	1.000
76: hard palate	1.300	14110	0.209E+02	0.161E+00	0.770E+01	1.000
77: cerebellum	1.040	82339	0.122E+03	0.113E+02	0.924E+02	12.000
78: tongue	1.040	14222	0.211E+02	0.325E+00	0.154E+02	2.000
81: horn of entricl	1.300	8813	0.131E+02	0.101E+00	0.770E+01	1.000
82: nasal septum	0.600	3420	0.508E+01	0.391E-01	0.770E+01	1.000
83: white matter	1.040	301514	0.448E+03	0.138E+02	0.308E+02	4.000
84: superior sagita	1.040	8379	0.124E+02	0.957E-01	0.770E+01	1.000
85: medulla entri	1.040	2355	0.350E+01	0.108E+00	0.308E+02	4.000
88: artificial lesi	1.040	2783	0.413E+01	0.382E+00	0.924E+02	12.000
89: frontal lobes	1.040	66601	0.989E+02	0.913E+01	0.924E+02	12.000
91: pons	1.040	13232	0.196E+02	0.181E+01	0.924E+02	12.000
92: third ventricle	1.040	5270	0.782E+01	0.602E-01	0.770E+01	1.000
95: occipital lobes	1.040	41438	0.615E+02	0.568E+01	0.924E+02	12.000
96: hippocampus	1.040	4218	0.626E+01	0.578E+00	0.924E+02	12.000
97: pituitary gland	1.040	51	0.757E-01	0.699E-02	0.924E+02	12.000
98: cerebral fluid	1.040	295805	0.439E+03	0.338E+01	0.770E+01	1.000
99: uncus(ear bones)	1.300	473	0.702E+00	0.540E-02	0.770E+01	1.000
100: turbinates	0.600	3820	0.567E+01	0.436E-01	0.770E+01	1.000
101: caudate nucleus	1.040	6239	0.926E+01	0.855E+00	0.924E+02	12.000
102: zygoma	1.040	5585	0.829E+01	0.128E+00	0.154E+02	2.000
103: insula cortex	1.040	7749	0.115E+02	0.106E+01	0.924E+02	12.000
104: sinuses/mouth c	0.600	101924	0.151E+03	0.233E+01	0.154E+02	2.000
105: putamen	1.040	6129	0.910E+01	0.840E+00	0.924E+02	12.000
106: optic nerve	1.040	936	0.139E+01	0.428E-01	0.308E+02	4.000
107: internal capsul	1.040	5478	0.813E+01	0.250E+00	0.308E+02	4.000
108: septum pellucid	1.040	528	0.784E+00	0.241E-01	0.308E+02	4.000
109: thalamus	1.040	7306	0.108E+02	0.100E+01	0.924E+02	12.000
110: eyeball	1.040	7644	0.113E+02	0.873E-01	0.770E+01	1.000
111: corpus collosum	1.040	6458	0.959E+01	0.295E+00	0.308E+02	4.000
112: special region	1.040	3874	0.575E+01	0.531E+00	0.924E+02	12.000
113: cerebral falx	1.040	2657	0.394E+01	0.121E+00	0.308E+02	4.000
114: temporal lobes	1.040	136441	0.203E+03	0.187E+02	0.924E+02	12.000
115: fourth entricle	1.040	1123	0.167E+01	0.128E-01	0.770E+01	1.000
116: frontal portion	1.040	3109	0.461E+01	0.710E-01	0.154E+02	2.000
117: parietal lobes	1.040	70899	0.105E+03	0.972E+01	0.924E+02	12.000

118: amygdala	1.040	2347	0.348E+01	0.322E+00	0.924E+02	12.000
119: eye	1.040	7930	0.118E+02	0.906E-01	0.770E+01	1.000
120: globus pallidus	1.040	2471	0.367E+01	0.339E+00	0.924E+02	12.000
121: lens	1.040	360	0.534E+00	0.411E-02	0.770E+01	1.000
122: cerebral aquadu	1.040	312	0.463E+00	0.356E-02	0.770E+01	1.000
123: lateral ventric	1.040	5648	0.838E+01	0.645E-01	0.770E+01	1.000
124: prefrontal lobe	1.040	31441	0.467E+02	0.431E+01	0.924E+02	12.000

Photon energy	Abundance
27.202 keV	0.2469
27.473 keV	0.4598
31.104 keV	0.1316
31.762 keV	0.2860E-01
158.970 keV	0.8325
174.200 keV	0.8300E-05
182.610 keV	0.1800E-03
192.170 keV	0.1990E-03
198.230 keV	0.3500E-04
206.790 keV	0.3300E-04
207.800 keV	0.1120E-04
247.960 keV	0.6980E-03
257.510 keV	0.1600E-04
278.360 keV	0.2300E-04
281.030 keV	0.7890E-03
295.170 keV	0.1582E-04
329.380 keV	0.2600E-04
330.700 keV	0.1164E-03
343.730 keV	0.4400E-04
295.170 keV	0.1582E-04
346.350 keV	0.1257E-02
405.020 keV	0.2980E-04
437.500 keV	0.7000E-05
440.020 keV	0.4229E-02
454.760 keV	0.4120E-04
505.330 keV	0.2660E-02
528.960 keV	0.1280E-01
538.540 keV	0.3788E-02

556.050 keV	0.2900E-04
562.790 keV	0.1150E-04
578.260 keV	0.1260E-04
599.690 keV	0.2660E-04
610.050 keV	0.1100E-04
624.570 keV	0.7980E-03
628.260 keV	0.1640E-04
687.950 keV	0.2690E-03
735.780 keV	0.6160E-03
783.590 keV	0.5910E-03
837.100 keV	0.5820E-05
877.520 keV	0.8300E-05
894.800 keV	0.1010E-04
909.120 keV	0.1410E-04
1036.630 keV	0.9700E-05
1068.120 keV	0.1420E-04

INTERACTIONS IN THE CRYSTAL

MaxValue spectrum..: 0.1566E+05

MaxValue projection: 1.116

CountRate spectrum.: 8575.

CountRate E-Window.: 3550.

PHOTONS AFTER COLLIMATOR AND WITHIN ENER-WIN

Geometric.....: 0.00 %	100.00 %
Penetration.....: 0.00 %	0.00 %
Scatter in collim..: 0.00 %	0.00 %
X-rays in collim...: 0.00 %	0.00 %

SCATTER IN ENERGY WINDOW

Scatter/Primary....: 0.26755

Scatter/Total.....: 0.21107

Scatter order 1....: 88.77 %

Scatter order 2....: 10.16 %

Scatter order 3....: 1.07 %

CALCULATED DETECTOR PARAMETERS

Efficiency E-Window: 0.3669

Efficiency spectrum: 0.8864

Sensitivity Cps/MBq: 34.1337

Sensitivity Cpm/uCi: 75.7768

Simulation started.: 2024:08:01 22:07:07

Simulation stopped.: 2024:08:02 01:03:21

Elapsed time.....: 2 h, 56 m and 14 s

DetectorHits.....: 16380809

DetectorHits/CPUsec: 1655

SIMIND built 2022:11:25 with INTEL Win compiler

Random number generator: ranmar

Comment:EMISSION VBRN

Energy resolution as function of 1/sqrtI

Header file: gelehrbrain39.h00

Inifile: simind.ini

Command: simind gelehrbrain39/fi:i123/fz:phantom

A.2 Reconstruction (OSEM)

PS C:\$Users >$ smc2castor gelehrbrain39.h00 gelehrbrain3916/ru/at/it:16/su:8/mb:5.2/sm:5

C:\$Users >$castor-recon -df gelehrbrain39.cdh -fout gelehrbrain3916 -it 16:8 -oit 16:16 -dim 128,128,128 -vox 2.00,2.00,2.00 -conf C:\ castor2\config\ -vb 1 -opti MLEM -proj classicSiddon -flip-out Y

$$sOutputManager :: InitOutputDirectory() -> Outputpathis'gelehrbrain3916'$$

$$oProjectorManager :: Initialize() -> Initializeprojectorsandprojectionlines$$

$$oOptimizerManager :: Initialize() -> Initializeoptimizerandpenalty$$

$$iOptimizerMLEM :: Initialize() -> UsetheMLEMoptimizer$$

$$oIterativeAlgorithm :: IterateCPU() -> Startalgorithm for 16 iterations$$

$$oIterativeAlgorithm :: IterateCPU() -> Startiteration 1/16 subset 1/8$$

$$oIterativeAlgorithm :: IterateCPU() -> Startiteration 1/16 subset 2/8$$

$$oIterativeAlgorithm :: IterateCPU() -> Startiteration 1/16 subset 3/8$$

$$oIterativeAlgorithm :: IterateCPU() -> Startiteration 1/16 subset 4/8$$

$$oIterativeAlgorithm :: IterateCPU() -> Startiteration 1/16 subset 5/8$$

$$oIterativeAlgorithm :: IterateCPU() -> Startiteration 1/16 subset 6/8$$

$$oIterativeAlgorithm :: IterateCPU() -> Startiteration 1/16 subset 7/8$$

$$oIterativeAlgorithm :: IterateCPU() -> Startiteration 1/16 subset 8/8$$

$$oIterativeAlgorithm :: IterateCPU() -> Startiteration 2/16 subset 1/8$$

$$oIterativeAlgorithm :: IterateCPU() -> Startiteration 2/16 subset 2/8$$

$$oIterativeAlgorithm :: IterateCPU() -> Startiteration 2/16 subset 3/8$$

$$oIterativeAlgorithm :: IterateCPU() -> Startiteration 2/16 subset 4/8$$

$$oIterativeAlgorithm :: IterateCPU() -> Startiteration 2/16 subset 5/8$$

$oIterativeAlgorithm :: IterateCPU() -> Startiteration2/16subset6/8$

$oIterativeAlgorithm :: IterateCPU() -> Startiteration2/16subset7/8$

$oIterativeAlgorithm :: IterateCPU() -> Startiteration2/16subset8/8$

$oIterativeAlgorithm :: IterateCPU() -> Startiteration3/16subset1/8$

$oIterativeAlgorithm :: IterateCPU() -> Startiteration3/16subset2/8$

$oIterativeAlgorithm :: IterateCPU() -> Startiteration3/16subset3/8$

$oIterativeAlgorithm :: IterateCPU() -> Startiteration3/16subset4/8$

$oIterativeAlgorithm :: IterateCPU() -> Startiteration3/16subset5/8$

$oIterativeAlgorithm :: IterateCPU() -> Startiteration3/16subset6/8$

$oIterativeAlgorithm :: IterateCPU() -> Startiteration3/16subset7/8$

$oIterativeAlgorithm :: IterateCPU() -> Startiteration3/16subset8/8$

$oIterativeAlgorithm :: IterateCPU() -> Startiteration4/16subset1/8$

$oIterativeAlgorithm :: IterateCPU() -> Startiteration4/16subset2/8$

$oIterativeAlgorithm :: IterateCPU() -> Startiteration4/16subset3/8$

$oIterativeAlgorithm :: IterateCPU() -> Startiteration4/16subset4/8$

$oIterativeAlgorithm :: IterateCPU() -> Startiteration4/16subset5/8$

$oIterativeAlgorithm :: IterateCPU() -> Startiteration4/16subset6/8$

$oIterativeAlgorithm :: IterateCPU() -> Startiteration4/16subset7/8$

$oIterativeAlgorithm :: IterateCPU() -> Startiteration4/16subset8/8$

$oIterativeAlgorithm :: IterateCPU() -> Startiteration5/16subset1/8$

$oIterativeAlgorithm :: IterateCPU() -> Startiteration5/16subset2/8$

$oIterativeAlgorithm :: IterateCPU() -> Startiteration5/16subset3/8$

$oIterativeAlgorithm :: IterateCPU() -> Startiteration5/16subset4/8$

$oIterativeAlgorithm :: IterateCPU() -> Startiteration5/16subset5/8$

$oIterativeAlgorithm :: IterateCPU() -> Startiteration5/16subset6/8$

$oIterativeAlgorithm :: IterateCPU() -> Startiteration5/16subset7/8$

$oIterativeAlgorithm :: IterateCPU() -> Startiteration5/16subset8/8$

$oIterativeAlgorithm :: IterateCPU() -> Startiteration6/16subset1/8$

$oIterativeAlgorithm :: IterateCPU() -> Startiteration6/16subset2/8$

$oIterativeAlgorithm :: IterateCPU() -> Startiteration6/16subset3/8$

$oIterativeAlgorithm :: IterateCPU() -> Startiteration6/16subset4/8$

$oIterativeAlgorithm :: IterateCPU() -> Startiteration6/16subset5/8$

$oIterativeAlgorithm :: IterateCPU() -> Startiteration6/16subset6/8$

$oIterativeAlgorithm :: IterateCPU() -> Startiteration6/16subset7/8$

$oIterativeAlgorithm :: IterateCPU() -> Startiteration6/16subset8/8$

$oIterativeAlgorithm :: IterateCPU() -> Startiteration7/16subset1/8$

$oIterativeAlgorithm :: IterateCPU() -> Startiteration7/16subset2/8$

$oIterativeAlgorithm :: IterateCPU() -> Startiteration7/16subset3/8$

$oIterativeAlgorithm :: IterateCPU() -> Startiteration7/16subset4/8$

$oIterativeAlgorithm :: IterateCPU() -> Startiteration7/16subset5/8$

$oIterativeAlgorithm :: IterateCPU() -> Startiteration7/16subset6/8$

$oIterativeAlgorithm :: IterateCPU() -> Startiteration7/16subset7/8$

$oIterativeAlgorithm :: IterateCPU() -> Startiteration7/16subset8/8$

$oIterativeAlgorithm :: IterateCPU() -> Startiteration8/16subset1/8$

$oIterativeAlgorithm :: IterateCPU() -> Startiteration8/16subset2/8$

$oIterativeAlgorithm :: IterateCPU() -> Startiteration8/16subset3/8$

$oIterativeAlgorithm :: IterateCPU() -> Startiteration8/16subset4/8$

$oIterativeAlgorithm :: IterateCPU() -> Startiteration8/16subset5/8$

$oIterativeAlgorithm :: IterateCPU() -> Startiteration8/16subset6/8$

$oIterativeAlgorithm :: IterateCPU() -> Startiteration8/16subset7/8$

$oIterativeAlgorithm :: IterateCPU() -> Startiteration8/16subset8/8$

$oIterativeAlgorithm :: IterateCPU() -> Startiteration9/16subset1/8$

$oIterativeAlgorithm :: IterateCPU() -> Startiteration9/16subset2/8$

$oIterativeAlgorithm :: IterateCPU() -> Startiteration9/16subset3/8$

$oIterativeAlgorithm :: IterateCPU() -> Startiteration9/16subset4/8$

$oIterativeAlgorithm :: IterateCPU() -> Startiteration9/16subset5/8$

$$oIterativeAlgorithm :: IterateCPU() -> Startiteration 9/16 subset 6/8$$

$$oIterativeAlgorithm :: IterateCPU() -> Startiteration 9/16 subset 7/8$$

$$oIterativeAlgorithm :: IterateCPU() -> Startiteration 9/16 subset 8/8$$

$$oIterativeAlgorithm :: IterateCPU() -> Startiteration 10/16 subset 1/8$$

$$oIterativeAlgorithm :: IterateCPU() -> Startiteration 10/16 subset 2/8$$

$$oIterativeAlgorithm :: IterateCPU() -> Startiteration 10/16 subset 3/8$$

$$oIterativeAlgorithm :: IterateCPU() -> Startiteration 10/16 subset 4/8$$

$$oIterativeAlgorithm :: IterateCPU() -> Startiteration 10/16 subset 5/8$$

$$oIterativeAlgorithm :: IterateCPU() -> Startiteration 10/16 subset 6/8$$

$$oIterativeAlgorithm :: IterateCPU() -> Startiteration 10/16 subset 7/8$$

$$oIterativeAlgorithm :: IterateCPU() -> Startiteration 10/16 subset 8/8$$

$$oIterativeAlgorithm :: IterateCPU() -> Startiteration 11/16 subset 1/8$$

$$oIterativeAlgorithm :: IterateCPU() -> Startiteration 11/16 subset 2/8$$

$$oIterativeAlgorithm :: IterateCPU() -> Startiteration 11/16 subset 3/8$$

$oIterativeAlgorithm :: IterateCPU() -> Startiteration11/16subset4/8$

$oIterativeAlgorithm :: IterateCPU() -> Startiteration11/16subset5/8$

$oIterativeAlgorithm :: IterateCPU() -> Startiteration11/16subset6/8$

$oIterativeAlgorithm :: IterateCPU() -> Startiteration11/16subset7/8$

$oIterativeAlgorithm :: IterateCPU() -> Startiteration11/16subset8/8$

$oIterativeAlgorithm :: IterateCPU() -> Startiteration12/16subset1/8$

$oIterativeAlgorithm :: IterateCPU() -> Startiteration12/16subset2/8$

$oIterativeAlgorithm :: IterateCPU() -> Startiteration12/16subset3/8$

$oIterativeAlgorithm :: IterateCPU() -> Startiteration12/16subset4/8$

$oIterativeAlgorithm :: IterateCPU() -> Startiteration12/16subset5/8$

$oIterativeAlgorithm :: IterateCPU() -> Startiteration12/16subset6/8$

$oIterativeAlgorithm :: IterateCPU() -> Startiteration12/16subset7/8$

$oIterativeAlgorithm :: IterateCPU() -> Startiteration12/16subset8/8$

$oIterativeAlgorithm :: IterateCPU() -> Startiteration13/16subset1/8$

$oIterativeAlgorithm :: IterateCPU() -> Startiteration13/16subset2/8$

$oIterativeAlgorithm :: IterateCPU() -> Startiteration13/16subset3/8$

$oIterativeAlgorithm :: IterateCPU() -> Startiteration13/16subset4/8$

$oIterativeAlgorithm :: IterateCPU() -> Startiteration13/16subset5/8$

$oIterativeAlgorithm :: IterateCPU() -> Startiteration13/16subset6/8$

$oIterativeAlgorithm :: IterateCPU() -> Startiteration13/16subset7/8$

$oIterativeAlgorithm :: IterateCPU() -> Startiteration13/16subset8/8$

$oIterativeAlgorithm :: IterateCPU() -> Startiteration14/16subset1/8$

$oIterativeAlgorithm :: IterateCPU() -> Startiteration14/16subset2/8$

$oIterativeAlgorithm :: IterateCPU() -> Startiteration14/16subset3/8$

$oIterativeAlgorithm :: IterateCPU() -> Startiteration14/16subset4/8$

$oIterativeAlgorithm :: IterateCPU() -> Startiteration14/16subset5/8$

$oIterativeAlgorithm :: IterateCPU() -> Startiteration14/16subset6/8$

$oIterativeAlgorithm :: IterateCPU() -> Startiteration14/16subset7/8$

$oIterativeAlgorithm :: IterateCPU() -> Startiteration14/16subset8/8$

$oIterativeAlgorithm :: IterateCPU() -> Startiteration15/16subset1/8$

$oIterativeAlgorithm :: IterateCPU() -> Startiteration15/16subset2/8$

$oIterativeAlgorithm :: IterateCPU() -> Startiteration15/16subset3/8$

$oIterativeAlgorithm :: IterateCPU() -> Startiteration15/16subset4/8$

$oIterativeAlgorithm :: IterateCPU() -> Startiteration15/16subset5/8$

$oIterativeAlgorithm :: IterateCPU() -> Startiteration15/16subset6/8$

$oIterativeAlgorithm :: IterateCPU() -> Startiteration15/16subset7/8$

$oIterativeAlgorithm :: IterateCPU() -> Startiteration15/16subset8/8$

$oIterativeAlgorithm :: IterateCPU() -> Startiteration16/16subset1/8$

$oIterativeAlgorithm :: IterateCPU() -> Startiteration16/16subset2/8$

$oIterativeAlgorithm :: IterateCPU() -> Startiteration16/16subset3/8$

$oIterativeAlgorithm :: IterateCPU() -> Startiteration16/16subset4/8$

$oIterativeAlgorithm :: IterateCPU() -> Startiteration16/16subset5/8$

$$oIterativeAlgorithm :: IterateCPU() -> Startiteration16/16subset6/8$$

$$oIterativeAlgorithm :: IterateCPU() -> Startiteration16/16subset7/8$$

$$oIterativeAlgorithm :: IterateCPU() -> Startiteration16/16subset8/8$$

$$oIterativeAlgorithm :: StepAfterSubsetLoop() -> Saveimageatiteration16$$

$$oIterativeAlgorithm :: IterateCPU() -> Totaltimespent|User : 3266sec|CPU : 3.266223e+003sec$$

REFERENCES

1. Library, S. P., "Brain spect images," tech. rep., Science Photo, August, 2024. https://www.sciencephoto.com/search?q=brain+spect.

2. Johansson, L., "Translational imaging research," in *Principles of Translational Science in Medicine* (Marcus, E. J., ed.), pp. 189–194, Philadelphia, PA: Elsevier Inc.: Academic Press, 2015.

3. Ljungberg, M., "Absolute quantitation of spect studies," *Seminars in Nuclear Medicine, WB Saunders*, Vol. 48, no. 4, pp. 348–358, 2018. 10.1053/j.semnuclmed.2018.02.009.

4. Rahman, M. G., M. M. Islam, T. Tsujikawa, Y. Kiyono, and H. Okazawa, "Count-based method for specific binding ratio calculation in [i-123] fp-cit spect analysis," *Annals of Nuclear Medicine*, Vol. 33, pp. 14–21, 2019. doi: 10.1007/s12149-018-1297-1.

5. Schober, O., F. Kiesslings, and J. Debus, eds., *Molecular Imaging in Oncology*, Springer Nature Switzerland AG: Springer Cham, 2020.

6. Khalil, M. M., ed., *Basic Sciences of Nuclear Medicine*, Springer Nature Switzerland AG: Springer Cham, 2021.

7. Richards, A., *Quantification accuracy for I-123 SPECT/CT studies using LEHR and me collimators: a Monte Carlo study.* PhD thesis, University of the Free State, Paarl, South Africa, 2021.

8. Ljungberg, M., *The SIMIND Monte Carlo Program Version 7.0*, Lund: Lund University, 2023.

9. Saito, S., K. Nakajima, J. Komatsu, T. Shibutani, H. Wakabayashi, H. Mori, A. Takata, K. Ono, and S. Kinuya, "Absolute quantitation of sympathetic nerve activity using [123i] metaiodobenzylguanidine spect-ct in neurology," *EJNMMI reports*, Vol. 8, no. 1, p. 15, 2024.

10. Sanders, J. C., T. Kuwert, J. Hornegger, and P. Ritt, "Quantitative spect/ct imaging of 177 lu with in vivo validation in patients undergoing peptide receptor radionuclide therapy," *Molecular Imaging and Biology*, Vol. 17, pp. 585–593, 2015.

11. Oliveira, F. P., Z. Walker, R. W. Walker, J. Attems, J. C. Castanheira, A. Silva, C. Oliveira, S. Vaz, M. Silva, and D. C. Costa, "23i-fp-cit spect in dementia with lewy bodies, parkinson's disease and alzheimer's disease: a new quantitative analysis of autopsy confirmed cases," *Journal of Neurology, Neurosurgery & Psychiatry*, Vol. 92, no. 6, pp. 662–667, 2021.

12. Darcourt, J., J. Booij, K. Tatsch, A. Varrone, T. V. Borght, Ö. L. Kapucu, K. Någren, F. Nobili, Z. Walker, and K. V. Laere, "Eanm procedure guidelines for brain neurotransmission spect using 123 i-labelled dopamine transporter ligands, version 2," *European Journal of Nuclear Medicine and Molecular Imaging*, Vol. 37, pp. 443–450, 2010.

13. Rahmim, A., and H. Zaidi, "Pet versus spect: strengths, limitations and challenges," *Nuclear Medicine Communications*, Vol. 29, no. 3, pp. 193–207, 2008.

14. QIBA, "Quantifying dopamine transporters with 123iodine labeled ioflupane in neurodegenerative diseases," tech. rep., QIBA Profile, September 2019. https://qibawiki.rsna.org/images/b/b5/002.QIBA_SPECT_Ioflupane_Profile_v2.0.2019_10_15.pdf.

15. Kiernan, J. A., "Anatomy of the temporal lobe," *Epilepsy Research and Treatment*, Vol. 2012, no. 1, p. 176157, 2012. doi: 10.1155/2012/176157.6.

16. Aytaç, B., "Improving the quantification accuracy of tc-99m mibi dual-phase parathyroid spect/ct: A monte carlo simulation study," Master's thesis, Bogazici University, Istanbul, Turkey, 2023.

17. Braak, H., and E. Braak, "Neuropathological staging of alzheimer-related changes," *Acta Neuropathologica*, Vol. 82, no. 4, pp. 239–259, 1991.

18. James, S. N., E. N. Manning, M. Storey, J. M. Nicholas, W. Coath, S. E. Keuss, D. M. Cash, C. A. Lane, T. Parker, A. Keshavan, and S. M. Buchanan, "Neuroimaging, clinical and life course correlates of normal-appearing white matter integrity in 70-year-olds," *Brain Communications*, Vol. 5, no. 5, p. fcad225, 2023.

19. Cherry, S. R., J. A. Sorenson, and M. E. Phelps, *Physics in Nuclear Medicine, 4th ed.*, Elsevier, 2012.

20. Graham, M. M., "Quantification of radiotracer uptakeinto tissue," in *Molecular Imaging* (Ross, B. D., and S. S. Gambhir, eds.), pp. 1613–1624, Iowa City, USA: Elsevier Inc.: Elsevier Inc., 1st ed. ed., 2021.

21. Hayashi, T., M. Mishina, M. Sakamaki, Y. Sakamoto, S. Suda, and K. Kimura, "Effect of brain atrophy in quantitative analysis of 123 i-ioflupane spect," *Annals of Nuclear Medicine*, Vol. 33, pp. 579–585, 2019.

22. Morphis, M., J. A. van Staden, H. du Raan, and M. Ljungberg, "Evaluation of iodine-123 and iodine-131 spect activity quantification: a monte carlo study," *EJNMMI Physics*, Vol. 8, pp. 1–20, 2021. doi: 10.1186/s40658-021-00407-1.38.

23. Lew, C., "Evaluating spect/ct quantification in clinical practice," tech. rep., Nuclear Medicine News & Stories, siemens.com/NMNS, 2019.

24. Katua, A., A. Ankrah, M. Vorster, A. van Gelder, and M. Sathekge, "Optimization of ordered subset expectation maximization reconstruction for reducing urinary bladder artifacts in single-photon emission computed tomography imaging," *World Journal of Nuclear Medicine*, Vol. 10, no. 01, pp. 3–8, 2011.

25. Kuo, P. H., N. Eshghi, S. Tinaz, H. Blumenfeld, E. D. Louis, and G. Zubal, "Optimization of parameters for quantitative analysis of 123i-ioflupane spect images for monitoring progression of parkinson disease," *Journal of Nuclear Medicine Technology*, Vol. 47, no. 1, pp. 70–74, 2019.

26. Auer, B., N. Zeraatkar, J. D. Beenhouwer, K. Kalluri, P. H. Kuo, L. R. Furenlid, and M. A. King, "Investigation of a monte carlo simulation and an analytic-based approach for modeling the system response for clinical i-123 brain spect imaging," *15th International Meeting on Fully Three-Dimensional Image Reconstruction in Radiology and Nuclear Medicine*, Vol. 11072, pp. 187–190, 2019.

27. Peters, S. B., N. R. van der Werf, M. Segbers, F. H. van Velden, R. Wierts, K. A. Blokland, M. W. Konijnenberg, S. V. Lazarenko, E. P. Visser, and M. Gotthardt, "Towards standardization of absolute spect/ct quantification: a multi-center and multi-vendor phantom study," *EJNMMI Physics*, Vol. 6, pp. 1–14, 2019.

28. Healthcare, G. E., "Infinia family: High-performance dual-detector imaging systems," brochure, GE Healthcare, 2006.

29. Healthineers, S., "Symbia t series system specifications," brochure, Siemens Healthineers, Siemens Medical Solutions USA, Inc., 2013.

30. Macey, D. J., and R. Marshall, "Absolute quantitation of radiotracer uptake in the lungs using a gamma camera," *Journal of Nuclear Medicine*, Vol. 23, no. 8, pp. 731–734, 1982.

31. Li, S., A. J. Sinusas, L. W. Dobrucki, and Y. H. Liu, "New approach to quantification of molecularly targeted radiotracer uptake from hybrid cardiac spect/ct: methodology and validation," *Journal of Nuclear Medicine*, Vol. 54, no. 12, pp. 2175–2181, 2013.

32. Oral, A., "Optimization of spect for parathyroid imaging with varying instrumentation parameters: A simulation study," Master's thesis, Bogazici University, Istanbul, Turkey, 2018.

33. Toossi, M. B., J. P. Islamian, M. Momennezhad, M. Ljungberg, and S. H. Naseri, "Simind monte carlo simulation of a single photon emission ct," *Journal of Medical Physics*, Vol. 35, no. 1, pp. 42–47, 2010. doi: 10.4103/0971-6203.55967.

34. Balestrini, S., S. Francione, R. Mai, L. Castana, G. Casaceli, D. Marino, L. Provinciali, F. Cardinale, and L. Tassi, "Multimodal responses induced by cortical stimulation of the parietal lobe: a stereo-electroencephalography study," *Brain*, Vol. 138, no. 9, pp. 2596–2607, 2015.

35. Healthineers, S., "Symbia t series spect/ct system specifications," brochure, Siemens Healthineers, Siemens Medical Solutions USA, Inc., 2019.

36. Healthcare, G. E., "Millennium mg nuclear imaging system: site preparation manual," review, G E Healthcare, 2006.

37. Healthineers, S., "Symbia intevo: Spect/ct that improves your image," brochure, Siemens Healthineers, Siemens Healthcare GmbH, 2019.

38. Kangasmaa, T., E. Hippeläinen, C. Constable, S. Turunen, and A. Sohlberg, "Quantitative monte carlo-based brain dopamine transporter spect imaging," *Annals of Nuclear Medicine*, Vol. 35, pp. 17–23, 2021.

39. Uribe, C. F., P. L. Esquinas, J. Tanguay, M. Gonzalez, E. Gaudin, J. M. Beauregard, and A. Celler, "Accuracy of 177 lu activity quantification in spect imaging: a phantom study," *EJNMMI Physics*, Vol. 4, no. 1, pp. 1–20, 2017. doi: 10.1186/s40658-016-0170-3.

40. Schepper, S. D., G. Gnanasegaran, J. C. Dickson, and T. V. den Wyngaert, "Absolute quantification in diagnostic spect/ct: the phantom premise," *Diagnostics*, Vol. 11, no. 12, p. 2333, 2021. doi: 10.3390/diagnostics11122333.

41. Allangba, K. N. P. G., A. K. Koutouan, A. Giuliano, Z. Traoré, and A. Traino, "Partial volume effect (pve) correction in single photon emission computed tomography (spect) imaging," *Radiation Science and Technology*, Vol. 9, no. 3, pp. 26–35, 2023.

42. Polo, I. O., "Evaluation of the scattered radiation components produced in a gamma camera using monte carlo method," *Revista Brasileira de Engenharia Biomédica*, Vol. 30, pp. 179–188, 2014. doi: 10.1590/rbeb.2014.015.

43. Mathew, L. O., and D. E. Hall, "I-123 uptake," tech. rep., StatPearls, https://www.ncbi.nlm.nih.gov/books/NBK549779/, 2023.

44. Bailly, M., G. L. Rouzic, G. Metrard, and M. J. Ribeiro, "Faster acquisition for dopamine transporter imaging using swiftscan step and shoot continuous spect without impairing visual and semiquantitative analysis," *Frontiers in Medicine*, Vol. 7, p. 235, 2020.

45. Nosaka, H., M. Onoguchi, H. Tsushima, M. Suda, S. Kurata, A. Onoma, and R. Murakawa, "Influence of brain atrophy using semiquantitative analysis in [123i] fp-cit single-photon emission computed tomography by a monte carlo simulation study," *Scientific Reports*, Vol. 12, no. 1, p. 168, 2022.

46. Oumar, A. A., and E. Erçelebi, "Assessment of an in-house phantom for the quality control of a clinical gamma camera," *Journal of X-ray Science and Technology*, Vol. 28, no. 3, pp. 461–470, 2020.

47. Islamian, J. P., M. T. B. Toossi, M. Momennezhad, S. R. Zakavi, and R. Sadeghi, "Monte carlo study of the effect of backscatter materail thickness on 99mtc source response in single photon emission computed tomography," *Iranian Journal of Medical Physics*, Vol. 10, no. 1, pp. 69–77, 2013.

48. "Single photon emission computed tomography (spect) imaging," tech. rep., Department of Radiology, University of Utah, August 2024. https://medicine.utah.edu/radiology/research/learn/spect.

49. Fakhri, G. E., S. C. Moore, P. Maksud, A. Aurengo, and M. F. Kijewski, "Absolute activity quantitation in simultaneous 123i/99mtc brain spect," *Journal of Nuclear Medicine*, Vol. 42, no. 2, pp. 300–308, 2001.

50. Zhu, Y. M., "Ordered subset expectation maximization algorithm for positron emission tomographic image reconstruction using belief kernels," *Journal of Medical Imaging*, Vol. 5, no. 4, pp. 044005–044005, 2018.

51. Masterson, M., "How to calculate error," tech. rep., Indeed Career Guide, May 2023. https://www.indeed.com/career-advice/career-development/how-to-calculate-error.

52. Berti, V., L. Mosconi, and A. Pupi, "Brain: Normal variations and benign findings in fdg pet/ct imaging," *PET Clin*, Vol. 9, pp. 129–140, 2014.

53. Luft, A. R., M. Skalej, J. B. Schulz, D. Welte, R. Kolb, and K. B

54. Wild, H. M., R. A. Heckemann, C. Studholme, and A. Hammers, "Gyri of the human parietal lobe: volumes, spatial extents, automatic labelling, and probabilistic atlases," *PloS one*, Vol. 12, no. 8, p. e0180866, 2017. doi: 10.1371/journal.pone.0180866.

55. Matesan, M., S. Gaddikeri, K. Longfellow, R. Miyaoka, S. Elojeimy, S. Elman, S. C. Hu, S. Minoshima, and D. Lewis, "I-123 datscan spect brain imaging in parkinsonian syndromes: utility of the putamen-to-caudate ratio," *Journal of Neuroimaging*, Vol. 28, no. 6, pp. 629–634, 2018. doi: 10.1111/jon.12530.

56. Quinn, B., Z. Dauer, N. Pandit-Taskar, H. Schoder, and L. T. Dauer, "Radiation dosimetry of 18f-fdg pet/ct: incorporating exam-specific parameters in dose estimates," *BMC Medical Imaging*, Vol. 16, pp. 1–11, 2016.

57. Kupitz, D., HWissel, J. Wuestemann, S. Bluemel, M. Pech, H. Amthauer, M. C. Kreissl, and O. S. Grosser, "Optimization of spect/ct imaging protocols for quantitative and qualitative 99m tc spect," *EJNMMI Physics*, Vol. 8, pp. 1–14, 2021.

58. Tunninen, V., T. Kauppinen, and H. Eskola, "Physical characteristics of collimators for dual-isotope imaging with 99m tc and 123 i," in *EMBEC & NBC 2017. EMBEC NBC 2017 2017. IFMBE Proceedings* (Eskola, H., O. Väisänen, J. Viik, and J. Hyttinen, eds.), Vol. 65, (Singapore), pp. 245–249, Springer, Singapore, 13 June 2018. doi: 10.1007/978-981-10-5122-7_62.

59. Buchert, R., C. Lange, T. S. Spehl, I. Apostolova, L. Frings, C. Jonsson, P. T. Meyer, and S. Hellwig, "Diagnostic performance of the specific uptake size index for semi-quantitative analysis of i-123-fp-cit spect: harmonized multi-center research setting versus typical clinical single-camera setting," *EJNMMI Research*, Vol. 9, pp. 1–13, 2019.

60. Tunninen, V., T. Kauppinen, and H. Eskola, "Optimization of 99m tc-sestamibi/123 i subtraction spect/ct protocol for parathyroid scintigraphy," in *EMBEC & NBC 2017. EMBEC NBC 2017 2017. IFMBE Proceedings* (Eskola, H., O. Väisänen, J. Viik, and J. Hyttinen, eds.), Vol. 65, (Singapore), pp. 847–851, Springer, Singapore, 13 June 2018. doi: 10.1007/978-981-10-5122-7_212.

61. Niñerola-Baizán, A., J. Gallego, A. Cot, P. Aguiar, F. Lomeña, J. Pavía, and D. Ros, "Optimization of the reconstruction parameters in [123i] fp-cit spect," *Physics in Medicine & Biology*, Vol. 63, no. 8, p. 085009, 2018. doi: 10.1088/1361-6560/aab799.